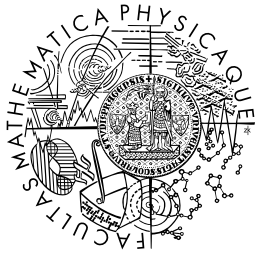

FACULTY
OF MATHEMATICS
AND PHYSICS
Charles University

MASTER THESIS

Brendan Ninneman

Subsolidus thermal convection as a key to understanding volatile evolution and internal dynamics of large icy bodies

Mathematics

Supervisor of the master thesis: RNDr. Klára Kalousová, Ph.D.

Study programme: Mathematics

Study branch: Mathematical Modeling in Physics and Technology

Prague 2020

I declare that I carried out this master thesis independently, and only with the cited sources, literature and other professional sources. It has not been used to obtain another or the same degree.

I understand that my work relates to the rights and obligations under the Act No. 121/2000 Sb., the Copyright Act, as amended, in particular the fact that the Charles University has the right to conclude a license agreement on the use of this work as a school work pursuant to Section 60 subsection 1 of the Copyright Act.

In ..... date ....

Author's signature

I dedicate this to my parents for their guidance throughout these years and trusting me to live in Europe. Also, I would like to thank the Tkacik family, the Csampai family, and the Cimalova family who all took care of me and gave me a home away from home. Thank you all.

I also dedicate this to my supervisor Klára, whose guidance and knowledge helped push me to understand more than I thought was possible.

Finally to Czech beer which is far better than United States beer.

Title: Subsolidus thermal convection as a key to understanding volatile evolution and internal dynamics of large icy bodies

Author: Brendan Ninneman

Mathematical Institute of Charles University: Mathematics

Supervisor: RNDr. Klára Kalousová, Ph.D., Department of Geophysics

Abstract: Titan is a unique moon in the solar system as it is the only one with a thick atmosphere, and surface lakes and seas. Observations made by the Cassini/Huygens probe showed the potential of a subsurface ocean hidden below the outer crust made of ice. This thesis analyzes the heat transfer through the crust of Titan to understand the long term evolution of the ocean. We developed a finite element model of the heat transfer through a thickening ice crust and investigated the effect of viscosity, internal heat flux, and ammonia concentration in the ocean. While other explanations cannot be ruled out, it was found high values of viscosity and possible ammonia presence could keep the ocean liquid for long periods.

Keywords: Titan, Thermal Convection, Heat Transfer, Finite Element Method

Contents

Introduction

Intelligent life let alone life itself located within the solar system and beyond is one of the main missions of both NASA and ESA. While hard evidence for life existing outside of Earth is still lacking, there are many prospects located within the solar system where primitive life may exist. One of these missions to search for the potential life was the Cassini-Huygens mission. This mission launched on October 15, 1997 on a seven year journey to Saturn. Cassini continued to explore the Saturn system for 13 years eventually meeting its end on September 15, 2017.

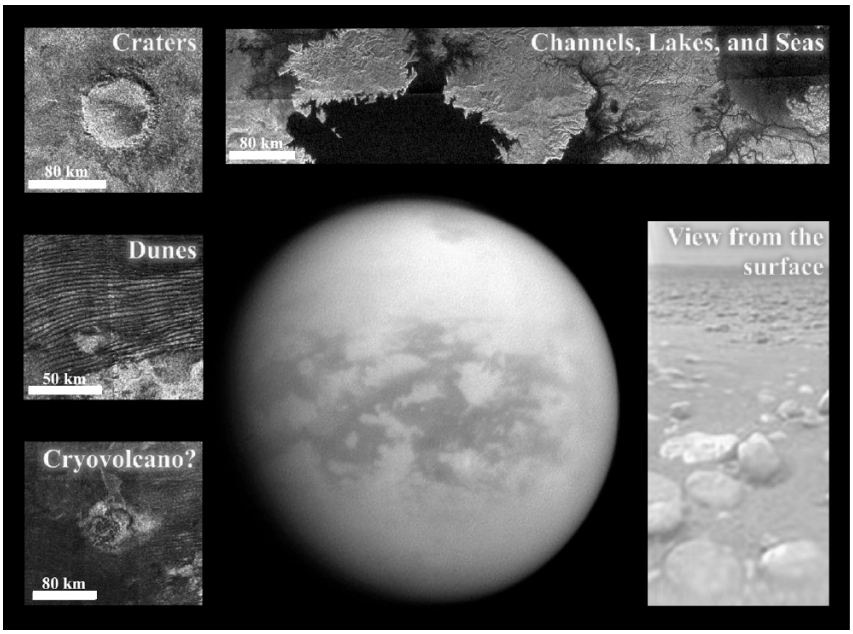

Figure 1: Titan's surface features (from *Hörst*, 2017).

While on its mission, the Cassini probe carried the Huygens landing module until its separation on December 25, 2004. The Huygens module landed on Titan on January 14, 2014 and returned data to Earth for the 90 minute decent. As the module descended through Titan's atmosphere it successfully sent 350 pictures. The atmosphere of Titan consists of roughly 97% nitrogen, 2.1% methane, and other complex organic molecules. The presence of methane in the atmosphere has brought up questions about its existence and how it is being supplied. The current level of methane should have been destroyed about 20-30 million years ago (*Yung et al.*, 1984). There is also observations of surface liquids on Titan in the form of lakes and seas primarily located in the North Pole (*Stofan et al.*, 2007). These surface observations also showed a geologically active and young surface showing resurfacing atmospheric processes. The pictures taken by Cassini show fluvial erosion features such as channels and rounded pebbles, dunes and other aeolian features and possible cryovolcanic showing active surface features as seen in Figure 1. On Titan the seasonal effects last on the timescale of Titan's year ($\sim$ 29.5 Earth years) were also observed, including the formation of clouds, and hydrocarbon precipitation (*Hörst*, 2017).

Both the probes returned a large amount of data concerning the composition of the atmosphere, as well as gravity, and shape measurements giving an insight

into the interior structure of Titan. Based on the data obtained by the Cassini probe, the interior of Titan is suggested to contain 4 spherical layers (cf. Figure 2): the silicate core, the layer of high-pressure phases of ice, the liquid ocean, and the outer ice I crust (*Iess et al.*, 2010; *Durante et al.*, 2019).

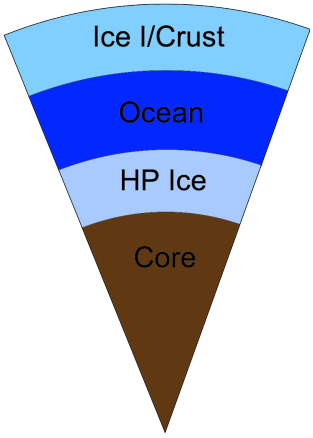

Figure 2: Interior structure of Titan

There are multiple pieces of evidence showing the existence of a liquid ocean. One piece of evidence is the Schumann resonance between ionosphere and lower conductive layer beneath non-conductive crust (*Béghin et al.*, 2012) which was measured by the descending Huygens module. Another evidence is the precise measurement of gravity field indicated a global layer within Titan behaves like a fluid on orbital time scales (*Iess et al.*, 2012). Finally, precise measurements of obliquity (the angle between satellite's rotational and orbital axis), are well explained by interior structure models with internal ocean (*Baland et al.*, 2014).

However, the long term stability of liquid ocean is not self-evident since the moon gradually looses its internal heat which comes mainly from the radiogenic decay in the silicate core. The internal heat is transferred through the different layers of the moon by heat diffusion or by advection before it is eventually lost by radiation into space. Being located just above the ocean, the ice crust governs the heat extraction and thus the ocean crystallization rate. If heat transfer through the crust is efficient, it is likely the ocean would freeze quickly. On the other hand, if the heat transfer through the crust is delayed by some mechanism, the ocean may still be liquid.

Some previous works, suggested some possibilities for the long term stability of the ocean. One of the suggested possibilities is the presence of an anti-freezer such as ammonia, that significantly lowers the crystallization temperature, thus slowing the crystallization (*Grasset and Sotin*, 1996). Another possibility is analyzing the viscous dissipation on the orbital timescales. This produces significant heating as in the case of Europa (*Sotin et al.*, 2009) and Enceladus (*Choblet et al.*, 2017). The third but not final possibility looks at a layer of insulating material on Titan's surface (*Tobie et al.*, 2006).

The goal of this thesis is to develop a model of heat transfer through the ice crust to address the long term stability of the ocean. In particular the primary focus will be to look at the effect of ammonia in the ocean proposed by *Grasset and Sotin* (1996). The structure of the thesis is as follows: first describe the concept

of the model and then derive the governing equations. Also describe the used numerical methods and the performed tests. In the second chapter, we present the obtained results which are compared in Discussion with the constraints on the likely parameter values that allow the longterm ocean stability. We also discuss the model assumptions and some implications of our results on the volatiles transfer. We conclude this thesis in the fourth chapter.

1. Model Formulation

1.1 Conceptual Model

The goal of this thesis will be to address the long term thermal stability of the ocean, by looking at the ocean's energy balance. The model will look at the parameters concerning the q_{in}, representing the incoming heat from the silicate core. This value is due to the radioactive decay of the silicates in the core. The next value to be analyzed is the q_{out} which is the heat extracted by the crust. Thus, comparing these two values, q_{out} and q_{in}, will determine if and when the ocean will freeze.

The q_{in}, will taken from previous models and assumptions based on the data from Titan. q_{out} this will be addressed by modeling the heat transfer through the crust, explained in section 1.3.6.

In the long term evolution of the model q_{out} will always be greater than q_{in}, thus the crust will crystallize. Therefore it becomes essential to solve the heat transfer through a crystallizing crust. For this purpose the idea of a dimensionless formulation with the following key ideas are used:

1. Heat flux coming from the interior, q_{in} is chosen (either constant or time dependent)

2. Heat transfer equations are solved in a non-dimensional box of a fixed thickness with the melting temperature prescribed at the bottom boundary. The melting temperature can evolve in time depending on the crust thickness and the ocean concentration

3. Based on the temperature field obtained in the previous step, the extracted heat flux q_{out} is evaluated

4. From the difference of q_{in} and q_{out}, the increase in physical thickness of the layer is computed from Stefan Law, Section 1.3.6. The corresponding quantities such as melting temperature (i.e. the bottom boundary condition) and the driving force (Rayleigh number, cf. Section 1.2.3) are reevaluated. Therefore, the bottom boundary condition as well as the driving force evolve in time through the simulation.

1.2 Equation Formulation

1.2.1 Derivation of Governing Equations

The balance laws are derived based on the principles of continuum mechanics following *Matyska* (2005). The following equations will be presented in their differential form except the internal energy balance equation which will be derived further.

The first equation presented is the mass balance equation

$$\frac{\partial \rho}{\partial t} + div(\rho \mathbf{v}) = 0. \tag{1.1}$$

The second equation presented is the linear momentum balance.

$$\frac{\partial \rho \mathbf{v}}{\partial t} + \nabla(\rho \mathbf{v} \otimes \mathbf{v}) = div\,(\mathbb{T}) + \mathcal{F}. \tag{1.2}$$

The equation has the following terms. The first term presented is the Cauchy stress,

$$\mathbb{T} = -p\mathbb{I} + \mathbb{T}^d. \tag{1.3}$$

The first part is the pressure dependence and the second part is the deviatoric part.

$$\mathbb{T}^d = \eta(\nabla \mathbf{v} + (\nabla \mathbf{v})^T). \tag{1.4}$$

With η representing the fluid viscosity.

Only considering gravity from the body forces, i.e. $\mathcal{F} = \rho \mathbf{g}$, the linear momentum balance equation reads

$$\frac{\partial \rho \mathbf{v}}{\partial t} + \nabla(\rho \mathbf{v} \otimes \mathbf{v}) = -\nabla p + div\left[\eta(\mathbf{v} + (\nabla \mathbf{v})^T)\right] + \rho \mathbf{g}. \tag{1.5}$$

From the angular momentum balance follows the symmetry of the Cauchy stress tensor:

$$\mathbb{T} = \mathbb{T}^T. \tag{1.6}$$

Finally, the internal energy balance can be expressed as:

$$\rho\left(\frac{\partial \varepsilon}{\partial t} + \mathbf{v} \cdot \nabla \varepsilon\right) = -div(\mathbf{q}) + \mathbb{T} : \nabla \mathbf{v} + Q. \tag{1.7}$$

With ε as the internal energy, q the heat flux, and Q as energy sources. A heat conducting fluid satisfying Fourier's Law is assumed giving the heat flux as

$$\mathbf{q} = -k \nabla \mathrm{T}. \tag{1.8}$$

Where k represents the thermal conductivity, and T as temperature. Using the Gibbs relation in the following form (e.g. *Martinec*, 2011) [1]

$$\rho \mathrm{T} \frac{Ds}{Dt} = \rho \frac{D\varepsilon}{Dt} + p div(\mathbf{v}). \tag{1.9}$$

with s the entropy, it is possible to rewrite 1.7 using both 1.8 and 1.9 to get

$$\rho T\left(\frac{\partial s}{\partial t} + \mathbf{v} \cdot \nabla s\right) = div(k \nabla \mathrm{T}) + \mathbb{T}^d : \nabla \mathbf{v} + Q. \tag{1.10}$$

The state of a fluid is determined by three variables: temperature, pressure and unit mass (density). These are not independent but are linked by the Equation of State (EoS), written as

$$f(p, \mathrm{T}, \rho) = 0. \tag{1.11}$$

[1] Where $\frac{D()}{Dt}$ is the material time derivative defined as

$$\frac{D()}{Dt} = \frac{\partial()}{\partial t} + \mathbf{v} \cdot \frac{\partial()}{\partial \mathbf{x}}.$$

but is usually seen in the following form

$$\rho = \tilde{\rho}(p, \mathrm{T}). \tag{1.12}$$

As a result only two variables: pressure and temperature, are independent. Then, we can express the entropy derivative as (e.g. *Matyska*, 2005)

$$\rho \mathrm{T} \frac{Ds}{Dt} = \rho \mathrm{T} \left(\frac{\partial s}{\partial \mathrm{T}} \right)\Big|_p \frac{D\mathrm{T}}{Dt} + \rho \mathrm{T} \left(\frac{\partial s}{\partial p} \right)\Big|_{\mathrm{T}} \frac{Dp}{Dt} = \rho c_p \frac{D\mathrm{T}}{Dt} - \alpha \mathrm{T} \frac{Dp}{Dt}. \tag{1.13}$$

with α representing the thermal expansivity and c_p the isobaric heat capacity. Assuming the dominance of the time-independent hydrostatic pressure p_0 given by

$$\nabla p_0 = \rho \mathbf{g}_0. \tag{1.14}$$

it is possible to write

$$\frac{Dp}{Dt} \approx \frac{Dp_0}{Dt} = \frac{\partial p_0}{\partial t} + \mathbf{v} \cdot \nabla p_0 = \rho \mathbf{g}_0 \cdot \mathbf{v} = -\rho g v_r. \tag{1.15}$$

where it is assumed $\mathbf{g} = -g\mathbf{e}_z$, where $\mathbf{e}_z$ is defined as the vertical direction unit vector. Resulting in the thermal equation

$$\rho c_p \frac{\partial \mathrm{T}}{\partial t} + \rho c_p \mathbf{v} \cdot \nabla \mathrm{T} = div(k \nabla \mathrm{T}) - \rho \alpha \mathrm{T} g v_r + \mathbb{T}^d : \nabla \mathbf{v} + Q. \tag{1.16}$$

The second term on the right hand side is interpreted as the adiabatic heating and is non-zero only if the vertical component of thermal gradient differs from the adiabatic gradient (cf. *Matyska*, 2005, for more details).

1.2.2 Boussinesq Approximation

The Boussinesq approximation works with a linearization of the conservation laws near a reference hydrostatic state when $\mathbf{v} = 0$. The main assumptions can be summarized as:

1. Linearization of the Equation of State with respect to the temperature variations from the reference state T_0:

   $$\rho = \rho_0(1 - \alpha(\mathrm{T} - \mathrm{T}_0)). \tag{1.17}$$

   where ρ_0 is constant (time and space - incompressible fluid)

2. Neglect of thermal expansion everywhere except in the gravity force

3. Splitting of pressure into the hydrostatic part and the dynamic pressure: $p = p_0 + \pi$ and subtracting the hydrostatic pressure gradient in the linear momentum balance

4. Neglecting the adiabatic heating, viscous dissipation and the internal energy source Q

Using these assumptions, it is possible to write the balance equations 1.1, 1.5, and 1.16 as:

$$div(\mathbf{v}) = 0. \tag{1.18}$$

$$\rho_0 \frac{D\mathbf{v}}{Dt} = -\nabla\pi + div\left[\eta\left(\nabla\mathbf{v} + (\nabla\mathbf{v})^T\right)\right] + \rho_0\alpha\left(\mathrm{T} - \mathrm{T}_0\right) g\mathbf{e}_z. \tag{1.19}$$

$$\rho_0 c_p \frac{\partial \mathrm{T}}{\partial t} + \rho_0 c_p \mathbf{v}\cdot\nabla\mathrm{T} = div\left(k\nabla\mathrm{T}\right). \tag{1.20}$$

1.2.3 Scaling (Non-dimensionalization)

To simplify the calculations, nondimensionalized variables are used. The following are used:

$$\mathbf{r} = D\mathbf{r}', \quad t = \frac{D^2}{\kappa}t', \quad \mathbf{v} = \frac{\kappa}{D}\mathbf{v}', \quad \pi = \frac{\eta_0\kappa}{D^2}\pi'$$
$$\eta = \eta_0\eta', \quad \mathrm{T} = \mathrm{T}_s + \Delta\mathrm{T}\mathrm{T}', \quad k = k_0 k'. \tag{1.21}$$

Here, D represents the characteristic dimension of the system, $\kappa = \frac{k_0}{\rho_0 c_p}$ the thermal diffusivity, η_0 the reference viscosity, k_0 the reference thermal conductivity, T_s the surface temperature, and $\Delta\mathrm{T} = \mathrm{T}_b - \mathrm{T}_s$ the temperature contrast across the layer (with T_b representing the temperature at the bottom). Using the variables 1.21, equations 1.18, 1.19, 1.20 can be rewritten as

$$div'(\mathbf{v}') = 0. \tag{1.22}$$

$$Pr^{-1}\frac{D\mathbf{v}'}{Dt'} = -\nabla'\pi' + div'\left[\eta'\left(\nabla'\mathbf{v}' + (\nabla'\mathbf{v}')^T\right)\right] + Ra\left(\mathrm{T}' - \mathrm{T}'_0\right)\mathbf{e}_z. \tag{1.23}$$

$$\frac{\partial \mathrm{T}'}{\partial t'} + \mathbf{v}'\cdot\nabla'\mathrm{T}' = div'\left(k'\nabla'\mathrm{T}'\right). \tag{1.24}$$

Two dimensionless numbers appear as a result of the nondimensionalization and are defined as:

$$Pr = \frac{\eta_0}{\rho_0\kappa}. \tag{1.25}$$

$$Ra = \frac{\rho_0\alpha g\Delta\mathrm{T}D^3}{\eta_0\kappa}. \tag{1.26}$$

The Prandtl number, equation 1.25, defines the ratio of momentum diffusivity to the thermal diffusivity. While the Rayleigh Number, equation 1.26, represents the ratio of thermal buoyancy to heat and momentum diffusion.

Table 1.1 shows the typical values of parameters that appear in Pr and Ra for the Earth's mantle and Titan's crust. The values of Pr and Ra are also given and show the left hand side of 1.23 can be safely neglected.

Table 1.1: Typical values of parameters

Variables	Earth's Mantle	Titan's Crust
η_0 (Pa s)	10^{21}	10^{13} - 10^{15}
ρ_0 (kg m^{-3})	$3.5 \cdot 10^3$	920
k_0 (W/m/K)	4	2.3
c_p (J/kg/K)	1100	2100
κ (m^2 s^{-1})	10^{-6}	$1.2 \cdot 10^{-6}$
α (K^{-1})	$3 \cdot 10^{-5}$	$1.6 \cdot 10^{-4}$
g (m s^{-2})	10	1.35
D (m)	$3 \cdot 10^6$	10^5
ΔT (K)	$3 \cdot 10^3$	170
Pr	10^{23}	10^{16} - 10^{18}
Ra	10^8	10^7 - 10^9

The Rayleigh number describes the behavior of fluid with mass anomalies due to a temperature contrast. If the Rayleigh number is above its critical value, the thermal buoyancy is strong enough to drive the fluid flow. Consequently, heat can be transferred by the flowing fluid and we speak of thermal convection. On the other hand, for small values of Ra (below the critical value), no fluid flow is observed and heat is only diffused by conduction. The Rayleigh number thus describes the driving force in the system of governing equations. In the model of heat transfer through the thickening ice crust, Ra will be increasing in time due to the increasing ice crust thickness D, cf. equation 1.26.

Thus, the final system of non-dimensional equations read:

$$\boxed{div(\mathbf{v}) = 0}. \tag{1.27}$$

$$\boxed{0 = -\nabla\pi + div\left[\eta\left(\nabla\mathbf{v} + (\nabla\mathbf{v})^T\right)\right] + Ra\,(\mathrm{T} - \mathrm{T}_0)\,\mathbf{e}_z}. \tag{1.28}$$

$$\boxed{\frac{\partial \mathrm{T}}{\partial t} + \mathbf{v}\cdot\nabla\mathrm{T} = div\,(k\nabla\mathrm{T})}. \tag{1.29}$$

Note: The primes are omitted for the sake of simplicity.

1.2.4 Specification of the Material Parameters

The two parameters specified in the non-dimensionalized equations (1.27, 1.28, 1.29), viscosity (η), and thermal conductivity (k) are significant in the variability they add to the governing equations.

Depending on the local stress-temperature conditions, ice deforms by various mechanism (diffusion creep, dislocation creep, grain boundary sliding, basal slip, *Goldsby and Kohlstedt* (2001)). In general, the rate of deformation by these mechanisms depends on three parameters, temperature, stress and ice grain size. Since temperature plays a dominant role in determining the viscosity value, we

only use volume diffusion, as it is the linear mechanism that depends only on temperature. Thus, the viscosity can be written as:

$$\eta\left(\mathrm{T}\right) = \eta_0 \exp\left(\frac{6 * 10^4}{8.314}\left(\frac{1}{\mathrm{T}} - \frac{1}{\mathrm{T}_{ref}}\right)\right). \tag{1.30}$$

The value of $6 \cdot 10^4$ J mol^{-1} is the thermal activation energy of ice, 8.314 J K^{-1} mol^{-1} is the gas constant, and T_{ref} is the reference temperature, chosen simply as the melting temperature of pure ice at low pressures. The prefactor η_0 is not well constrained and can vary over several orders of magnitude

To understand the importance of viscosity, Figure 1.1 plots the horizontal average of temperature (left) and the corresponding viscosity (right)

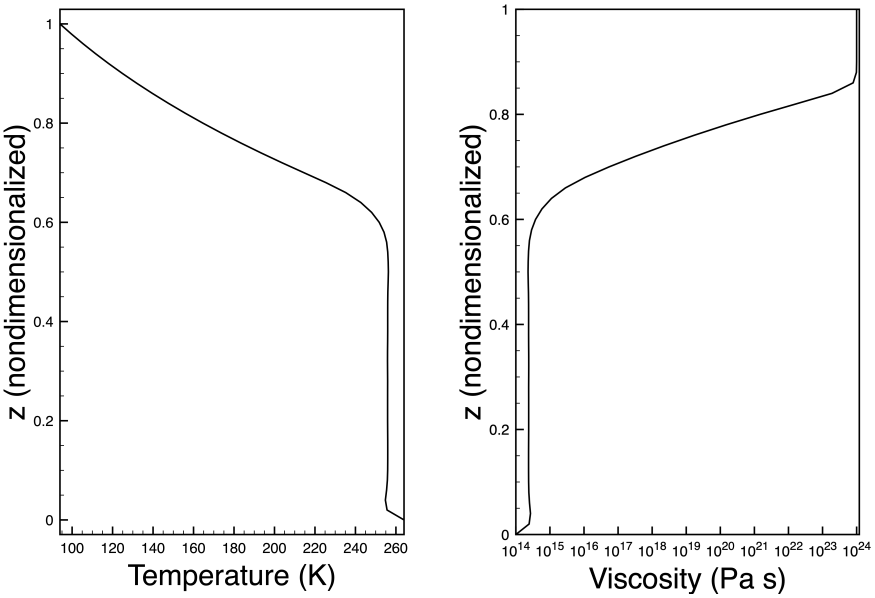

Figure 1.1: Depth dependence of horizontal temperature average (left) and the corresponding viscosity (right)

It is important to notice the strong dependence of viscosity shown in the equation 1.30 and the visualization in Figure 1.1. In terms of a physical representation, a low viscosity value seen on the right panel of Figure 1.1 on the left side ($z < 0.6$), results in more movement.

It is important to note the sharp vertical line on the right hand side of the right panel of Figure 1.1 ($z > 0.8$). This line corresponds to a cut-off value. For this model a cut-off of 10^{10} from the initial value was used. The use of the cut-off viscosity value is motivated by both, physical and numerical reasons. For the former, the high viscosity values that would be obtained without the use of cut-off for the low surface temperatures, would lead to extremely large values of stress which are well above the strength of the material. In order to avoid the use of a more complicated rheology that would include plastic deformation, the simple cut-off is used. As a result of the strong temperature dependence of viscosity, the cold part at the top of the layer stays rigid and does not participate in convection. This is defined as the stagnant lid.

Regarding the value of η_0, it depends on the ice grain size which is not known for the conditions within the ice moon's interior. The values used in this thesis,

10^{13} - 10^{15} Pa s, correspond to measurements performed on the Earth's glaciers (*Hudleston*, 2015).

The next material parameter is thermal conductivity ($k(\mathrm{T})$) defined as below:

$$k(\mathrm{T}) = \frac{488.12}{\mathrm{T}} + 0.4685. \tag{1.31}$$

with the values coming from *Hobbs* (1974).

To understand the importance of thermal conductivity, the plots of horizontal temperature average and the corresponding conductivity are shown below in Figure 1.2. Note that the conductivity at the surface is more than two times larger than the bottom conductivity.

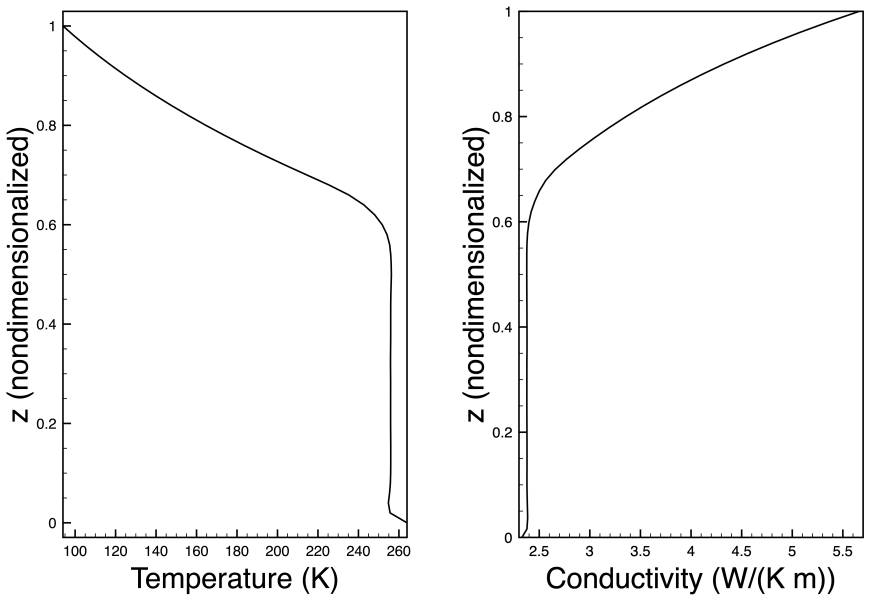

Figure 1.2: Depth dependence of horizontal temperature average (left) and corresponding conductivity (right)

Figure 1.3 shows a typical image of temperature field of a convecting fluid in the stagnant lid regime.

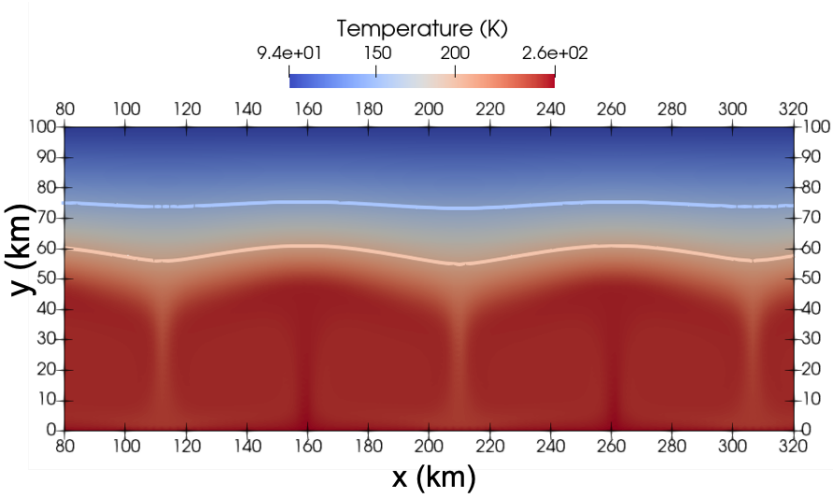

Figure 1.3: Basic image of convection. Hot material (red) tends to flow upwards forming the hot plumes (dark red). At the surface, the material is cold (blue) and due to the strong temperature dependence of viscosity does not partipate in the flow. This is what is called the stagnant lid. The two isocontours mark the temperatures of 150 and 200 K. Note, only a part of the computational domain is plotted here

1.3 Numerical Implementation

1.3.1 Boundary Conditions

To begin solving the governing equations it becomes necessary to look at the formulation and the boundary conditions. In this model the following boundary conditions are prescribed:

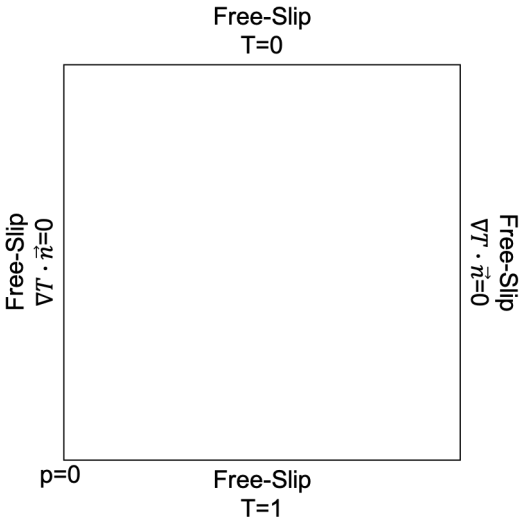

Figure 1.4: Initial domain Ω used with prescribed boundary conditions

As seen in the above Figure 1.4, free slip is prescribed on all boundaries for the mechanical problem. Free slip is defined as $\mathbf{v} \cdot \mathbf{n} = 0$, and $(\mathbb{T} \cdot \mathbf{n})_t = 0$ (with

$(\cdot)_t$ denoting the tangential part of the vector). Free slip in the physical sense is at the interface between a fluid and a stationary wall, the normal component of velocity is zero (i.e. no material flow across the boundary is allowed). On the other hand, the tangential component of the flow is unrestricted (tangential component of boundary traction is zero). Also note pressure is fixed to zero at the bottom left corner of the computational domain.

Regarding the temperature boundary conditions, the side boundaries are insulating (i.e. no heat will flow through the boundaries): $\nabla \mathrm{T} \cdot \mathbf{n} = 0$, while the top and bottom boundaries have a prescribed temperature value. As for the prescribed values, since the model involves a non-dimensionalized system $\mathrm{T}_S = 0$, representing the top temperature boundary and $\mathrm{T}_B = 1$ representing the bottom temperature boundary are used. Giving some dimensional values the top boundary value is 94 K, and the bottom value is 264 K.

1.3.2 Weak Formulation

To begin solving the PDE numerically, it is necessary to take in account the classical solution may not always exist. As a result, it becomes necessary to search for the weak solution. This is done by combining the PDE and a test function and integrating over the domain of Ω. In the following equations, φ_π, $\boldsymbol{\varphi}_v$, φ_T will denote the test functions, associated with the equations for pressure (π), velocity ($\mathbf{v}$), and temperature (T), respectively.

The first equation is the mass balance equation 1.27:

$$\int_\Omega (div \mathbf{v}) \ \varphi_\pi \ d\mathbf{x} = 0. \tag{1.32}$$

The second equation is the linear momentum balance equation 1.28.

$$\int_\Omega -\nabla\pi \cdot \boldsymbol{\varphi}_v + div\left(\eta\left[(\nabla\mathbf{v}) + (\nabla\mathbf{v})^T\right]\right) \cdot \boldsymbol{\varphi}_v + Ra\,(\mathrm{T} - \mathrm{T}_0)\,\mathbf{e}_z \cdot \boldsymbol{\varphi}_v \ d\mathbf{x} = 0. \tag{1.33}$$

employing product rule and applying Green's theorem to the first two terms of 1.33:

$$-\int_\Omega \nabla\pi \cdot \boldsymbol{\varphi}_v d\mathbf{x} = \int_\Omega \pi div(\boldsymbol{\varphi}_v) d\mathbf{x} - \int_{\partial\Omega} \pi \boldsymbol{\varphi}_v \cdot \mathbf{n} \ dS. \tag{1.34}$$

$$\begin{aligned}
\int_\Omega div\left(\eta\left[\nabla\mathbf{v} + (\nabla\mathbf{v})^T\right]\right) \cdot \boldsymbol{\varphi}_v \ d\mathbf{x} &= -\int_\Omega \eta[\nabla\mathbf{v} + (\nabla\mathbf{v})^T] : \nabla\boldsymbol{\varphi}_v \ d\mathbf{x} \\
&\quad + \int_\Omega div\left[\eta\left(\nabla\mathbf{v} + (\nabla\mathbf{v})^T\right) \cdot \boldsymbol{\varphi}_v\right] \ d\mathbf{x} \\
&= -\int_\Omega \eta\left[\nabla\mathbf{v} + (\nabla\mathbf{v})^T\right] : \nabla\boldsymbol{\varphi}_v \ d\mathbf{x} \\
&\quad + \int_{\partial\Omega} \mathbf{n} \cdot \eta\left[\nabla\mathbf{v} + (\nabla\mathbf{v})^T\right] \cdot \boldsymbol{\varphi}_v \ dS.
\end{aligned} \tag{1.35}$$

The boundary term in 1.34, is equal to zero because of the free-slip Dirichlet condition ($\boldsymbol{\varphi}_v \cdot \mathbf{n} = 0$). In equation 1.35, the boundary term vanishes because the tangential part of traction $\left(\mathbf{n} \cdot \eta\left(\nabla\mathbf{v} + (\nabla\mathbf{v})^T\right)\right)$ and the normal component of test function $\boldsymbol{\varphi}_v$. Therefore their dot product is zero.

So taking in account the boundary terms vanish, results in the final equation for the weak formulation of the linear momentum balance:

$$\int_\Omega \pi \; div(\boldsymbol{\varphi}_v) \; d\mathbf{x} - \int_\Omega \eta \left[\nabla \mathbf{v} + (\nabla \mathbf{v})^T\right] : \nabla \boldsymbol{\varphi}_v \; d\mathbf{x} + \int_\Omega Ra \, (\mathrm{T} - \mathrm{T}_0) \, \mathbf{e}_z \cdot \boldsymbol{\varphi}_v d\mathbf{x} = 0. \quad (1.36)$$

Finally, multiplying the energy balance equation 1.29 by the test function and integrating over the whole domain gives:

$$\int_\Omega \frac{\partial \mathrm{T}}{\partial t} \varphi_\mathrm{T} + \mathbf{v} \cdot \nabla \mathrm{T} \; \varphi_\mathrm{T} d\mathbf{x} = \int_\Omega div(k(\mathrm{T}) \; \nabla \mathrm{T}) \varphi_\mathrm{T} \; d\mathbf{x}. \quad (1.37)$$

Employing product rule on the right hand side and Green's theorem as seen in 1.34 and 1.35:

$$\begin{aligned} \int_\Omega div(k(\mathrm{T}) \nabla \mathrm{T}) \varphi_\mathrm{T} d\mathbf{x} &= - \int_\Omega k(\mathrm{T}) \nabla \mathrm{T} \cdot \nabla \varphi_\mathrm{T} \; d\mathbf{x} + \int_\Omega div(k(\mathrm{T}) \nabla \mathrm{T} \varphi_\mathrm{T}) \; d\mathbf{x} \\ &= - \int_\Omega k(\mathrm{T}) \nabla \mathrm{T} \cdot \nabla \varphi_\mathrm{T} \; d\mathbf{x} + \int_{\partial\Omega} k(\mathrm{T}) \varphi_\mathrm{T} \nabla \mathrm{T} \cdot \mathbf{n}. \; dS \end{aligned} \quad (1.38)$$

The boundary integral in equation 1.38 vanishes due to the Dirichlet boundary condition at the bottom and top boundary ($\varphi_\mathrm{T} = 0$). Also, due to the zero heat flux at the side boundaries ($\nabla \mathrm{T} \cdot \mathbf{n} = 0$). Thus resulting in the final weak formulation:

$$\int_\Omega \frac{\partial \mathrm{T}}{\partial t} \varphi_\mathrm{T} + \mathbf{v} \cdot \nabla \mathrm{T} \varphi_\mathrm{T} \; d\mathbf{x} = - \int_\Omega k(\mathrm{T}) \; \nabla \mathrm{T} \cdot \nabla \varphi_\mathrm{T} d\mathbf{x}. \quad (1.39)$$

1.3.3 Space and Time Discretization

The system of governing equations is solved in two steps: first, the energy balance (eq. 1.39) is solved to update the temperature using the velocities from the previous time step. Then, the Stokes system (eqs. 1.32, 1.36) is solved using the updated temperature. Thus the following function spaces are used:

$$\begin{aligned} \mathcal{P} &:= \left\{ \pi \in L^2(\Omega); \int_\Omega \pi d\mathbf{x} = 0 \right\}, \\ \mathcal{V} &:= \left\{ \mathbf{v} \in H^1(\Omega); \; \int_{\partial\Omega} (\mathbb{T}^d \cdot \mathbf{n})_t \; dS = 0 \right\}, \\ \mathcal{T} &:= \left\{ \mathrm{T} \in H^1(\Omega); \int_{\partial\Omega_{\text{(Left and Right)}}} \nabla \mathrm{T} \cdot \mathbf{n} \; dS = 0 \right\}. \end{aligned}$$

To discretize the Stokes problem, the Taylor-Hood elements were initially used (*Taylor and Hood*, 1973). This method uses ($\mathcal{P}^2$, $\mathcal{P}^1$) elements for the velocity and pressures spaces, satisfying the Babuška-Brezzi [2]condition. Below are the

element spaces used

$$P = \left\{ \varphi_\pi \in C\left(\overline{\Omega}\right);\ \varphi_\pi|_K \in \mathcal{P}^1(K)\ \forall K \in \mathcal{Q}_h;\ \int_\Omega \varphi_\pi\ d\mathbf{x} = 0 \right\},$$
$$\mathbf{V} = \left\{ \boldsymbol{\varphi}_v \in C\left(\overline{\Omega}\right);\ \boldsymbol{\varphi}_v|_K \in \mathcal{P}^2(K)\ \forall K \in \mathcal{Q}_h;\ \int_{\partial\Omega} \boldsymbol{\varphi}_v \cdot \mathbf{n}\ dS = 0 \right\}.$$

To solve the energy balance, piecewise quadratic element space is used for the temperature space, defined as:

$$T = \{\varphi_{\mathrm{T}} \in C\left(\overline{\Omega}\right);\ \varphi_{\mathrm{T}}|_K \in \mathcal{P}^2(K)\ \forall K \in \mathcal{Q}_h; \int_{\partial\Omega_{(\text{Top and Bottom})}} \varphi_{\mathrm{T}}\ dS = 0\}.$$

Where $\mathcal{P}^q$ are polynomials of degree q. Linear Lagrange elements are used, i.e. for the pressure space (P), where the degrees of freedom correspond to evaluation of the polynomial at the vertices. While in the velocity space ($\mathbf{V}$) and temperature space (T), the evaluation is performed at the vertices and in the middle of the triangle's sides.

The theta scheme is used to solve the heat balance equation with $\theta = 1/2$, thus corresponding to the Crank-Nicolson method. The time-step (Δt) is controlled by the Courant-Friedrichs-Lewy (CFL) criterion. This criterion is used so the distance information travels in each time step is lower than the distance between the mesh elements. Thus, information from one cell is only allowed to propagate to its immediate neighbors.

Combining this with 1.32, 1.36, and 1.39 and the elements listed above gives the final system of equations:

$$\begin{aligned}
0 &= \int_\Omega div(\mathbf{v})\ \varphi_\pi + \pi\ div(\boldsymbol{\varphi}_v) - \eta(\mathrm{T})\left[\nabla\mathbf{v} + (\nabla\mathbf{v})^T\right] : \nabla\boldsymbol{\varphi}_v + Ra\ (\mathrm{T} - \mathrm{T}_0)\,(\mathbf{e}_z \cdot \boldsymbol{\varphi}_v)\ d\mathbf{x}, \\
0 &= \int_\Omega \frac{1}{\Delta t}(\mathrm{T}_n - \mathrm{T}_{n-1})\varphi_{\mathrm{T}} + \theta\left((\mathbf{v}\cdot\nabla\mathrm{T}_n)\,\varphi_{\mathrm{T}} + k(\mathrm{T}_{n-1})\,(\nabla\mathrm{T}_n \cdot \nabla\varphi_{\mathrm{T}})\right) \\
&\quad + (1-\theta)\left((\mathbf{v}\cdot\nabla\mathrm{T}_{n-1})\,\varphi_{\mathrm{T}} + k(\mathrm{T}_{n-1})\nabla\mathrm{T}_{n-1}\cdot\nabla\varphi_{\mathrm{T}}\right)\ d\mathbf{x}.
\end{aligned} \tag{1.40}$$

In the previous notation the subscripts n and $n-1$ correspond to the current and previous time step, respectively. It is important to note in equations 1.40, by taking the conductivity value from the previous step ($k(\mathrm{T}_{n-1})$) in both the implicit and explicit terms in the θ scheme results in the linearized form of the energy balance.

Thus in the weak formulation, 1.40, by taking π, $\mathbf{v}$, $\mathrm{T} \in ((\mathcal{P}\times\mathcal{V})\times\mathcal{T})$ in which is initially solved for the energy balance, then solved for the Stokes system. To help with the solving of numerical system and the weak formulation, the FEniCS software was used ((*Logg et al.*, 2012; *Alnæs et al.*, 2015)).

[2]Also known as the inf-sup condition satisfying,

$$\inf_{q_h \neq 0 \in M_{h0}} \sup_{\mathbf{v}_h \neq 0 \in \mathbf{X}_{h0}} \frac{(q_h, div_h \mathbf{v}_h)}{||q_h||\ |||\mathbf{v}_h|||_h} \geq \beta$$

1.3.4 Blankenbach Benchmark

To validate the implementation, the Blankenbach benchmark test is used (*Blankenbach et al.*, 1989). The test involves the steady isoviscous convection in a square box, which is heated from below and cooled from above. During the benchmark test, two values were collected

Nusselt Number

$$Nu = -\frac{\int_0^1 \frac{\partial \mathrm{T}}{\partial z}(z=1)\ dx}{\int_0^1 T(z=0)\ dx}. \tag{1.41}$$

This first equation represents the heat-flux over the top boundary divided by the temperature on the bottom boundary. The second value characterizes the efficiency of heat transfer by:

root mean square velocity (v_{rms})

$$v_{rms} = \left[\int_0^1 \int_0^1 \left(v_x^2 + v_z^2\right)^{1/2} dzdx\right]. \tag{1.42}$$

This value represents the v_{rms} of the entire domain Ω. The benchmark test looks at three different benchmark cases, however only the following two benchmark cases were done:

1. Isoviscous convection, with three Rayleigh numbers $(10^4, 10^5, 10^6)$
2. Convection with temperature, dependent viscosity according to the following equation ($b = \ln(1000)$)

$$\eta = \eta_0 \exp\left[-\frac{b\mathrm{T}}{\Delta \mathrm{T}}\right]. \tag{1.43}$$

In the previous equation 1.43, the b constant represents the viscosity contrast over the layer of three-orders of magnitude.

Below are the results vs the benchmark values used for the box domain as described in Figure 1.4. The first figure looks at the Blankenbach benchmark test 1a with a $Ra = 10^4$.

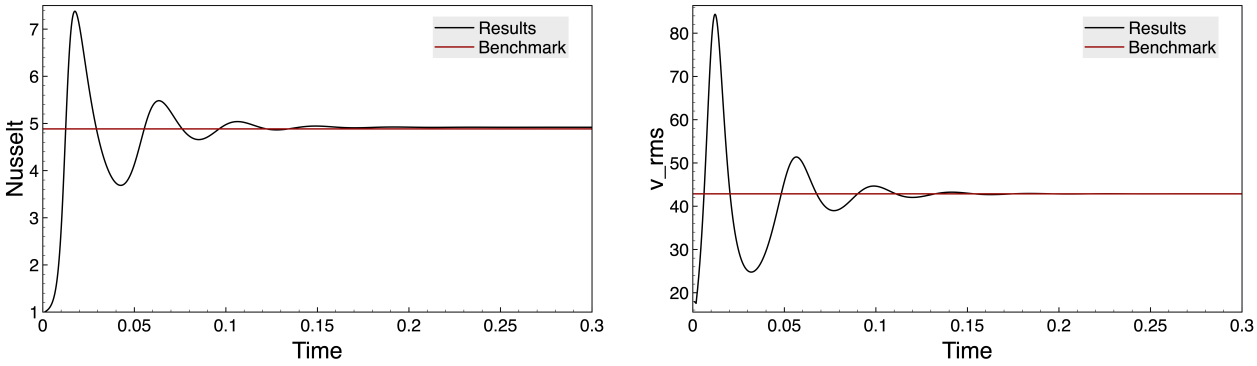

Figure 1.5: Blankenbach Benchmark test 1a (10^4), left: Nusselt number, right: rms velocity

What is evident in the benchmark values vs the tested values in Figures 1.5, the evolution of the Nusselt number and the v_{rms} is time dependent, but in the end when the computational domain reaches a steady state it establishes at the benchmark value. The next figure analyzes an increase in the Ra number to 10^5 and comparing it against the benchmark value.

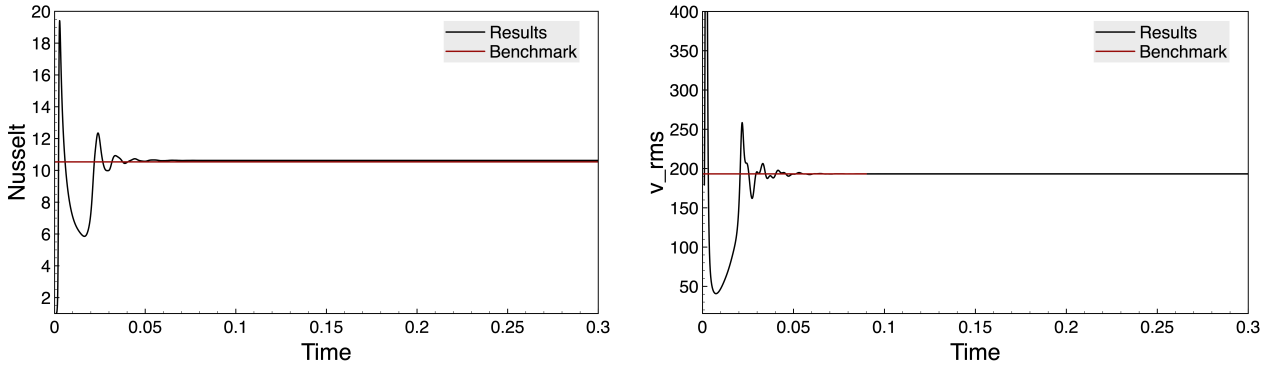

Figure 1.6: Blankenbach Benchmark test 1b (10^5), left: Nusselt number, right: rms velocity

Comparing the benchmark values in Figures 1.6, the evolution of the Nusselt number and the v_{rms} again are time-dependent. However, the simulation eventually reaches a steady state and establishes the benchmark values. Noting the difference between the Figures 1.5 and 1.6, it is noticeable the increase in v_{rms} and the Nusselt number. This is due to the increase in the Ra as defined by equation 1.26, causing the flow to become faster and the heat transfer is more efficient. The next simulation will look at increasing Ra by another order of magnitude and comparing the simulation values against the well established benchmark.

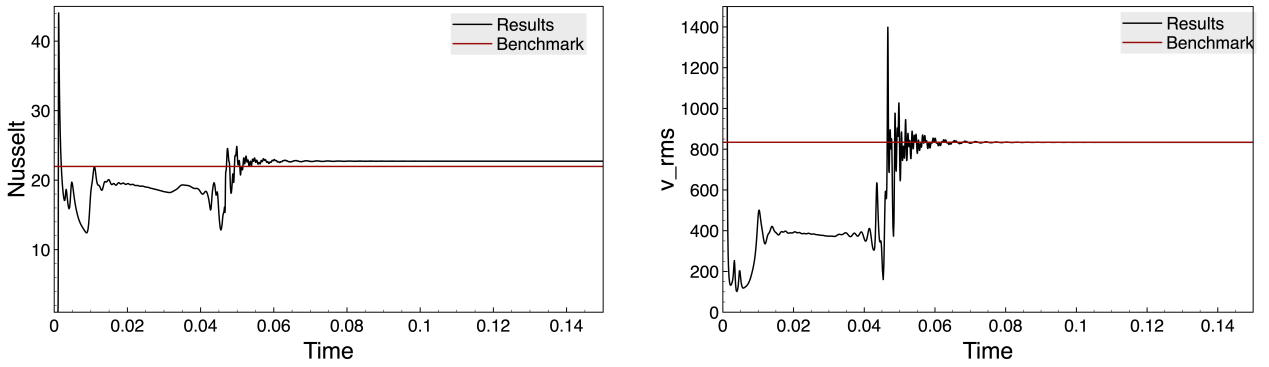

Figure 1.7: Blankenbach Benchmark test 1c (10^6), left: Nusselt number, right: rms velocity

Comparing the final simulation of the Blankenbach benchmark test 1c against the simulation, it is evident the Nusselt number and the v_{rms} are again time-dependent, and when the simulation reaches the steady state, the values approach the established benchmark values. Noticing the difference between the v_{rms} and Nusselt number values in Figure 1.6 and 1.7, it is evident again the high dependence of the v_{rms} and the Nusselt number on the Ra.

The final comparison of the code running against the Blankenbach test looks at the temperature dependence of viscosity defined by equation 1.43.

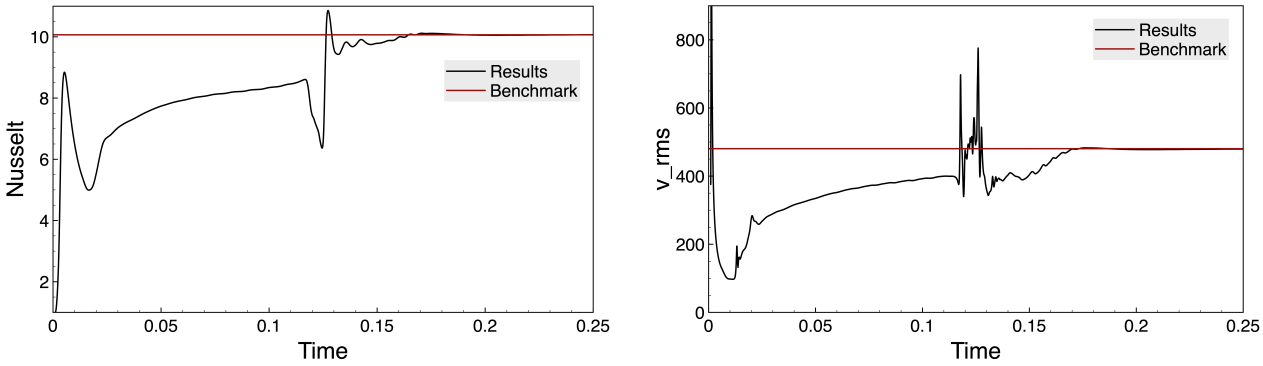

Figure 1.8: Blankenbach Benchmark test 2a, left: Nusselt number, right: rms velocity

In this final benchmark test, with the temperature dependent viscosity with a contrast of 3 orders of magnitude over the layer. The simulation takes a longer time to achieve the steady state solution, however the steady state values of the Nusselt number as well as the rms velocity are again in good agreement with the benchmark values. Performing the tests successfully defined by *Blankenbach et al.* (1989), verifies the implementation of thermal convection with constant as well as temperature dependent viscosity.

1.3.5 Mini-Elements

Long computational times resulted while using the Taylor-Hood method when we ran some basic simulations of Titan. These long times are due to the large number of degrees of freedom associated with the Taylor-Hood method. The mini element method was considered to reduce the number of degrees of freedom as described in *Arnold et al.* (1984).

The idea of the mini element is to stabilize the unstable pair ($\mathcal{P}^1$, $\mathcal{P}^1$) by adding a bubble function to the velocity space. To do this it becomes necessary to define new spaces to replace the Taylor-Hood velocity element:

$$\mathbf{V}' = \{\boldsymbol{\varphi}_v = \boldsymbol{\varphi}_b + \boldsymbol{\varphi}_u \ : \ \boldsymbol{\varphi}_b \in \mathbf{B} \ , \ \boldsymbol{\varphi}_u \in \mathbf{U}\} .$$

Where $\mathbf{B}$ is the bubble element space and $\mathbf{U}$ is the linear velocity element space, which are defined as:

$$\mathbf{B} = \left\{\boldsymbol{\varphi}_b \in C\left(\overline{\Omega}\right) ; \ \boldsymbol{\varphi}_b|_K \in \mathcal{P}^3(K) \ \forall K \in \mathcal{T}_h ; \ \boldsymbol{\varphi}_b|_{\partial\mathcal{T}_h} = 0\right\} ,$$
$$\mathbf{U} = \left\{\boldsymbol{\varphi}_u \in C\left(\overline{\Omega}\right) ; \ \boldsymbol{\varphi}_u|_K \in \mathcal{P}^1(K) \ \forall K \in \mathcal{T}_h ; \ \int_{\partial\Omega} \boldsymbol{\varphi}_u \cdot \mathbf{n} \, dS = 0 \right\} .$$

The bubble element ($\mathbf{B}$) evaluates the degrees of freedom at different points than the Lagrange element. For this particular choice $q = 3$ (cubic bubble element), the evaluation point is located in the barycenter of the triangular element.

Thus, using this new velocity space, we look for the solution of the previous problem with the same formulation, π, $\mathbf{v}$, T $\in ((P \times \mathbf{V}') \times T)$. The method of solving the system is the same as before by solving for the energy balance and then solving the Stokes system with the included bubble element.

To verify if the results obtained with the new velocity space agrees with the previous solution obtained with the Taylor-Hood elements, a few test simulations were run. This is shown in the panels of Figure 1.9

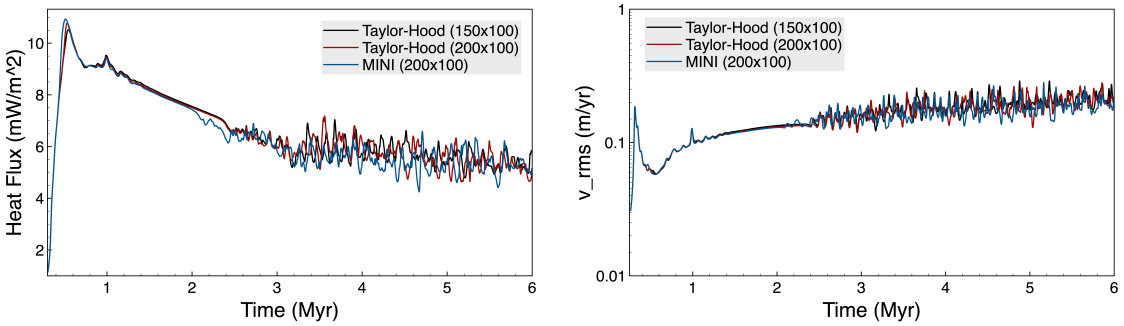

Figure 1.9: Comparison of the solutions obtained with Taylor-Hood Elements on mesh with 200x100 elements (red) and 150x100 elements (black) with the solution obtained with the Mini Elements on mesh with 200x100 elements (blue), left: heat flux, right: rms velocity

The left panel of Figure 1.9 shows the heat flux through the bottom boundary as a function of time for Taylor-Hood elements (red) and Mini elements (blue). The plots look at the results evaluated on a mesh of 200x100 elements with a domain of length two and height one. While the lines are not exactly the same, the overall amount of heat transferred is the same. The right panel shows the time evolution of the rms velocity for the two different elements choice and indicates the two solutions agree. Finally, a different mesh resolution was used with 150x100 elements resulting in a slightly flattened elements (with a length to height ratio of 1.3:1). The corresponding results are show in black and indicate that this slight change in the element shape does not have an effect on the overall result.

1.3.6 Crystallization / Crust Thickening

As mentioned in the Introduction, the crust crystallizes on long time scales. This section describes the implementation of the crystallization process. The crystallization rate Γ can be evaluated using the Stefan law:

$$\Gamma = \frac{\Delta q}{L\rho}. \tag{1.44}$$

In the above equation Δq is the difference in the heat fluxes at the ocean/ice interface, L is the latent heat of freezing for H_2O ($3.33 \cdot 10^5 \frac{J}{kg}$), and ρ is the density of ice. The Stefan problem describes the evolution of the interface between different phases (ice and water) over time. In this case, the solidification of water into ice or the melting of ice into water.

The model also assumes there is no dissipation in the ocean. Therefore, the heat coming from the silicate core is only transferred by the ocean and does not change. The heat flux is defined as $\Delta q = q_i - q_s$, where the q_i, the heat extracted from the ocean by the crust, while the q_s is the value for the heat flux provided by the interior silicate core. The figures in 1.10 give a visual representation of the Stefan problem.

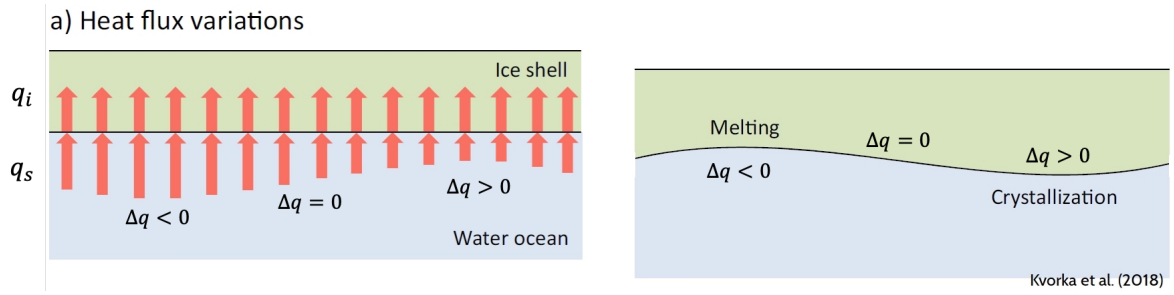

Figure 1.10: left: heat flux variations, right: phase changes, Figure modified from *Kvorka et al.* (2018)

To give an idea of crystallization in the model, if $\Delta q > 0$ then, this would imply the heat extracted by the ice crust is greater than the heat supplied from the silicates resulting in crystallization. This is evident in the left panel of Figure 1.10, on the right hand side, and the corresponding to the right hand side of the right panel of figure 1.10. On the other hand if $\Delta q < 0$ then, the heat extracted by the ice crust is smaller than the heat supplied by the silicate core resulting in melting as seen on the left-hand side of the left panel of figure 1.10 and the left-hand side of the right panel of 1.10.The final important case is when $\Delta q = 0$. In this case the heat extracted by the ice crust is exactly the same as the heat supplied, so there is no change in the ice crust thickness. This is evident in right panel of 1.10, in the middle of the picture where there is not change in the ice crust thickness.

Since the interest is in the long term evolution of the whole ice crust and not the local ice crust thickness variations, the heat extracted by the ice crust (q_i) is taken as an average over the bottom boundary:

$$q_i = \left| -\frac{1}{l} \int_{\Gamma_b} k(\mathrm{T}) \nabla \mathrm{T} \cdot \mathbf{n} ds \right|. \tag{1.45}$$

In the above equation, l represents the width of the computational domain. Also, Γ_b represents the bottom boundary, and $k(\mathrm{T})$ is the heat conductivity defined by Equation 1.31. Thus, Equation 1.45, analyzes the heat flux through the boundary and takes the average over the entire boundary. In order to implement the change in thickness of the ice crust, the change is computed in each time step as $\Delta D = \frac{\Delta q}{L\rho} \Delta t$, increasing D in every time step. Thus changing the Rayleigh number 1.26 depending on the thickness and corresponding the change of the driving force.

Now, the focus will shift to the effect of the mesh resolution and domain aspect ratio (length to height) on simulations with a prescribed constant crystallization rate. Figure 1.11, shows the results of simulations with different aspect ratios and mesh resolutions.

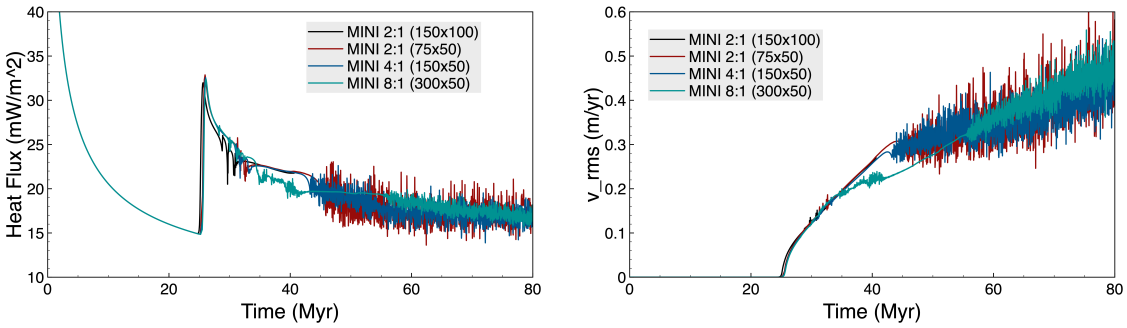

Figure 1.11: Comparison of results obtained with aspect ratio 2 and mesh resolution 150x100 (black), aspect ratio 2 and coarser mesh with 75x50 (red), aspect ratio 4:1 and mesh resolution of 150x50 (blue), and aspect ratio 8 and mesh resolution of 300x50 elements (green). Left: Bottom heat flux, Right: rms velocity

First, comparing the effects of former mesh resolution of 150x100 (black) and coarser mesh with 75x50 elements (red). Both the basal heat flux (left) and the rms velocity (right) show the same time for the onset of convection ($\sim$ 25 Myr) and the same trend in the evolution indicating the vertical resolution of 50 elements should be enough for the simulations with increasing thickness. Note even for the thickest crusts ($<$ 200 km), this corresponds to an element size of less than 4 km.

The next test involved looking at the effect of aspect ratios (2, 4, 8) while keeping the same vertical resolution (50 elements) and the same shape of the elements (1.3:1). Both the heat flux and the rms velocity again show the same evolution in time suggesting the aspect ratio does not have a significant effect on the results. Therefore it was decided to use the domain aspect ratio of 4 with the mesh resolution of 150x50 in the rest of the thesis.

1.3.7 Effect of Pressure and Ammonia on Melting Temperature

As explained in the model definition, the temperature of the bottom boundary is the melting temperature which in general depends on both, the pressure (given by the ice crust thickness, $P = \rho g D$) and the composition of the ocean. Since ammonia will stay in the liquid and will not be trapped in the crystallizing ice, the ammonia concentration in the ocean will increase during crystallization. Due to the large hydrosphere thickness, a layer of high-pressure (HP) ice polymorphs will probably crystallize at the interface of the ocean and the silicate core. To obtain a correct estimate of the ammonia concentration in the ocean, it becomes necessary to have an estimate of the ocean volume. Since the model only provides the ice crust thickness (D), the question of parameterizing the HP ice layer thickness in terms of D. Figure 1.12 investigates this question.

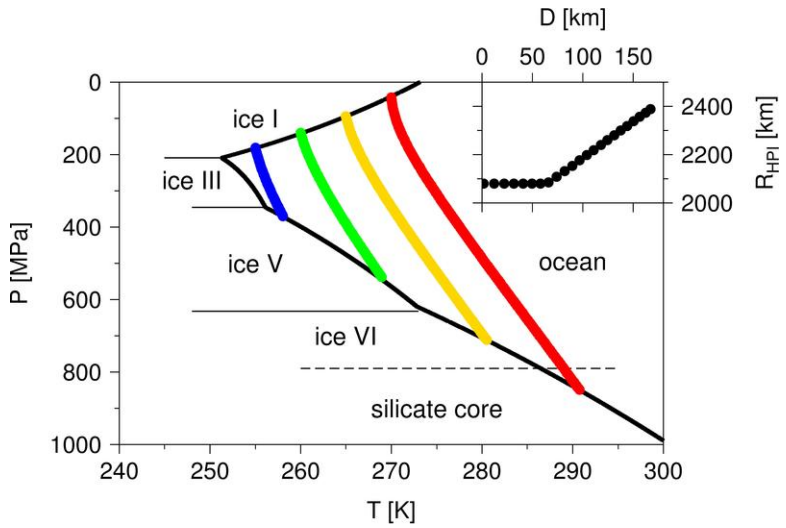

Figure 1.12: Pressure-Temperature Diagram of H_2O. the thick black line indicates the melting curve, while the thin black lines show the phase transitions between the different ice phases. The dashed line marks the pressure at the interface between the silicate core and the hydrosphere. The colored lines represent possible temperature profiles in the ocean (cf. text for more details). The inlet figure shows the radius of the HP ice / ocean interface.

Figure 1.12, shows the pressure-temperature diagram for Titan's conditions. The black line represents a pure H_2O melting temperature. To the right of the black line this represents the liquid phase of H_2O or as in the case of the model, the ocean. The left side of the thick line represents the different ice phases resulting from different pressures. The thin black lines represent the transitions between these ice phases. The dashed line near the bottom of the diagram represents the boundary between Ice VI and the silicate core, which in Titan's case is on average 2080 km from the center. As a result any of the colored lines to the right from where the dashed line meets the solid black-line, no HP Ice will form.

The colored lines show four different temperature profiles for four different thicknesses of ice crust $D = 30$ km (red), 80 km (yellow), 110 km (green), 150 km (blue). The profiles follow the adiabatic gradient in the ocean and their intercept with the melting curve indicates the radius of the HP ice / ocean interface. By this process, the ocean-HP ice interface R_{HPI} can be found for any thickness of the outer ice crust D. The corresponding values are plotted in the inlet figure and it became possible to derive the following scaling to describe the ocean-HP ice interface radius:

$$\begin{aligned} R_{HPI}\ [km] &= 2080 & D &< 65\ km, \\ R_{HPI}\ [km] &= 1885 + 3D & D &\geq 65\ km. \end{aligned} \tag{1.46}$$

Thus in equation 1.46, the radius of the HP ice / ocean interface (and therefore the thickness of the HP Ice) depends strictly on the crust thickness. If the crust has a thickness of less than 65 km, then there is no HP Ice. However, if the value is above 65 km then HP ice layer starts to crystallize. Thus, the thickening of the crust and the HP Ice leads to a decrease in the volume of the ocean which is important when implementing the ammonia concentration in the ocean.

Thus when the concentration of ammonia in the ocean increases, results in higher values as the simulation continues. Thus to calculate the amount of ammonia in the ocean, first the dependence of the HP ice layer to the ice crust thickness D is used as in equation 1.46. Then the mass of the ocean is calculated as:

$$M_{oc} = \frac{4\pi\rho_{oc}}{3}\left(R_{Ice}^3 - R_{HPI}^3\right). \tag{1.47}$$

Where, ρ_{oc} represents the density of water, $R_{Ice} = R_{Titan} - D$, where R_{Titan} is the radius of Titan (2575 km), and R_{HPI} is the computed radius of the HP Ice / ocean interface by equation 1.46. The current concentration in the ocean is given by:

$$X = \frac{X_0 M_{oc_0}}{M_{oc}}. \tag{1.48}$$

With X_0, the initial ammonia concetration, and M_{oc_0} is the initial ocean mass. Thus, with the inclusion of ammonia in the ocean results in a change in the melting temperature of H_2O, represented in the following equation (*Leliwa-Kopystyński et al.*, 2002):

$$T(P,X) = 273.1 - 7.95{\cdot}10^{-8}P - 9.6{\cdot}10^{-17}P^2 - 53.8X - 650X^2 - 4{\cdot}10^{-8}PX. \tag{1.49}$$

Thus, to implement change in the melting temperature, the Dirichlet bottom boundary condition is modified every time step. It is important to notice the dependence of both pressure and concentration in the ocean to the melting temperature of the bottom ice crust layer. Using equation 1.49, for certain ammonia concentration values is shown in Figure 1.13:

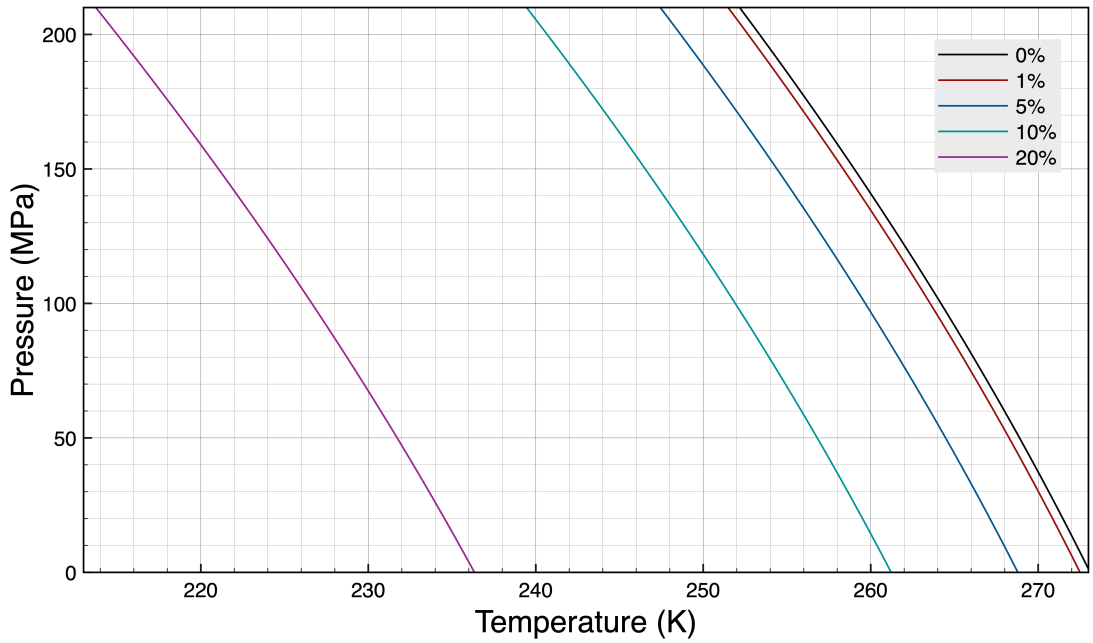

Figure 1.13: Melting temperature for pressures between 0 and 210 MPa (triple point ice I - ice III - liquid) and different values of ammonia concentration

In Figure 1.13, it is important to note taking the values to the right of each of the lines is ocean while to the left is Ice I. At the top of the diagram represents roughly 210 MPa, which is the triple point between Ice I, liquid, Ice III. To note some of the values associated with the diagram, looking at the 0% concentration (black line), starts at the bottom of 0 MPa with a melting temperature of roughly 273.1 K. As we continue to increase in pressure to 210 MPa, the value decreases to 252.2 K. This would be the value if there was a 0% ammonia concentration in the ocean. With each added percentage of ammonia, it is evident the melting temperature decreases significantly.

1.3.8 Expected Interior Heat Fluxes

The heat coming from the interior of Titan is mainly due to the radiogenic decay in the core.

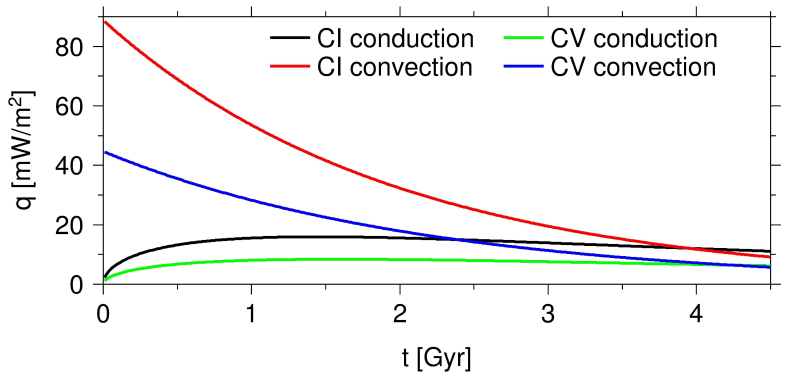

Figure 1.14: Models of time evolution of interior heat flux (*Kalousová and Sotin*). CI and CV indicate different composition of the core while conduction and convection indicate the different means of heat transfer in the core (cf. text for more details)

Figure 1.14, shows the possible time evolution of heat flux from Titan's interior. Since the exact composition of Titan's core is not know, it is often assumed similar to the composition of chondrites that represent the material from the early solar system. For Figure 1.14, two types of chondrites were chosen: ivuna type (CI) and chondrites vigarano type (CV). These represent the potentially different compositions of the core of Titan. CI chondrites are a form of meteorites possessing the strongest similarity to the distribution of the original solar nebula. CV are more dense, and less porous than CI. It is important to note typically CI have more radiogenic elements. In Figure 1.14, this explains why the CI heat flux is larger than the CV heat flux. They are made of interstellar grains that are older than the Earth.

Thus in Figure 1.14, the lines represent the heat flux from the silicate core q_s as explained in section 1.3.6. Thus, the typical radiogenic decay depicted if the core is convecting is shown if the major core concentration contains CI (red), or CV (blue). However, if the core is conducting then the q_s values represented by the following CI (black), or CV (green). Conduction slowly increases initially is due to the slow efficiency of heat transfer. Thus it takes more time to reach the bottom of the ice crust. Figure 1.14, this is a model of expected heat fluxes.

Thus the expected values in the early days of Titan are 20-40 mW/m^2, while 5-10 mW/m^2 are representative of present day Titan.

2. Results

In the results sections, the first section, section 2.1, will look at a crust with a fixed thickness and therefore constant in time bottom temperature. Thus, understanding the effects of thickness and the reference viscosity. The next section, section 2.2, will analyze a thickening crust and later look at the effects of viscosity and ammonia composition in the ocean.

2.1 Thermal Convection in Titan's Crust with Fixed Thickness

A reference simulation is important in determining how changing variables will result in different outcomes. Thus, the reference simulation for this model will have a fixed thickness, 100 km and an initial viscosity of $\eta_0 = 10^{14}$ Pa s. These values are chosen to understand a reference convection regime to changing the thickness (D) convection regime or initial viscosity (η_0) convection regime. This is evident in the two panels of Figure 2.1:

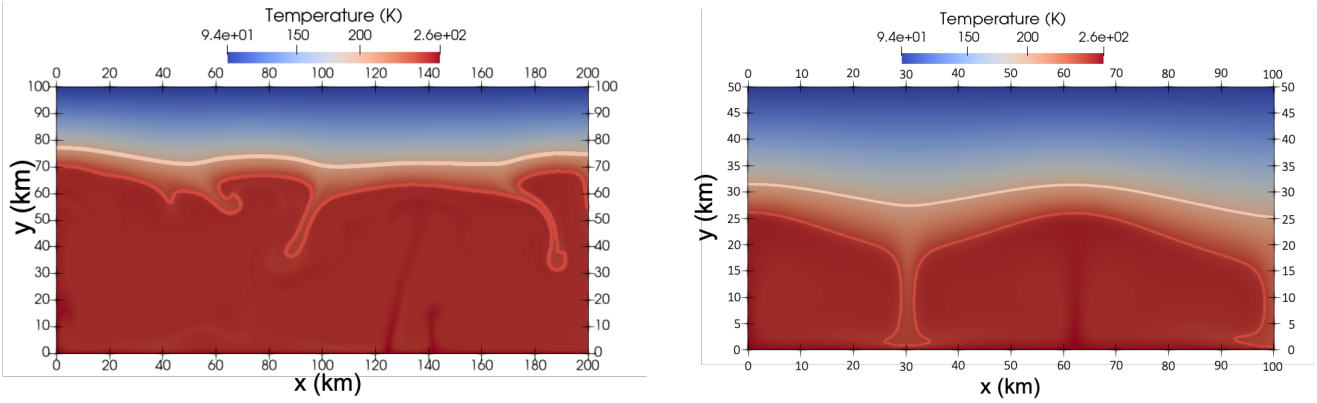

Figure 2.1: Comparison between convection patterns seen in the reference configuration (left) and D = 50 km (right). Simulation has elements of (200x100). The top line in both panels represents a contour of T = 200 K and the bottom line represents a contour of T = 250 K

As a basic convection image as seen in both panels of Figure 2.1, the dark red plumes represent the hot material at the bottom. The darker red material represents the inside of a plume which is hotter than the surrounding material. The material at the bottom is forced upward by convection eventually hitting the cold blue material at the top. The cold material at the top is known as the stagnant lid, in which warm material is not able to move past. This is due to strong temperature dependence of viscosity as seen in Figure 1.1.

Looking at the two figures above, Figure 2.1, it is noticeable the difference between the convection regimes at the end of the simulation. The 50 km thick crust has a stable pattern in time, while the 100 km thick crust is more vigorous and chaotic.

Using the reference configuration parameter of initial viscosity, $\eta_0 = 10^{14}$ Pa

s, but changing the initial thickness of the ice crust, Figure 2.2 investigates this idea.

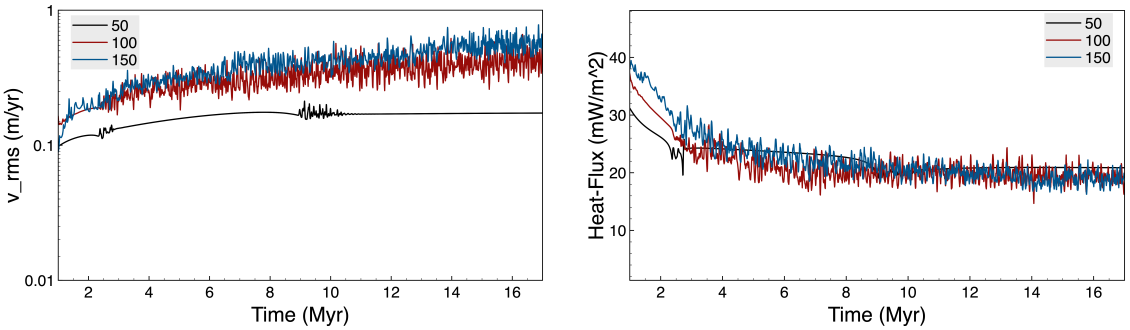

Figure 2.2: Effect of the Crust Thickness (D), rms velocity (left) and bottom heat flux (right) time evolution

In the left panel of Figure 2.2, it is important to note the log values on the y-axis. It becomes evident in the left panel of Figure 2.2, due to the cubic dependence of thickness in the Ra as seen in equation 1.26, thickness is one of the driving forces to determining the efficiency and turbulence of the flow. As seen in the right panel of Figure 2.1, in the 50 km case, there is a stable plume in time. However, as thickness increases (100 km and 150 km) the plumes become more chaotic in time and lose the uniformity. Also the flow efficiency in the 100 km and 150 km simulations are seen in left panel of Figure 2.2, where the rms velocity (v_{rms}) is higher compared to the 50 km case. The amount of extracted heat is comparable for all three thicknesses (right).

The next figure will investigate three initial viscosity values (η_0) with a constant uniform thickness of 100 km:

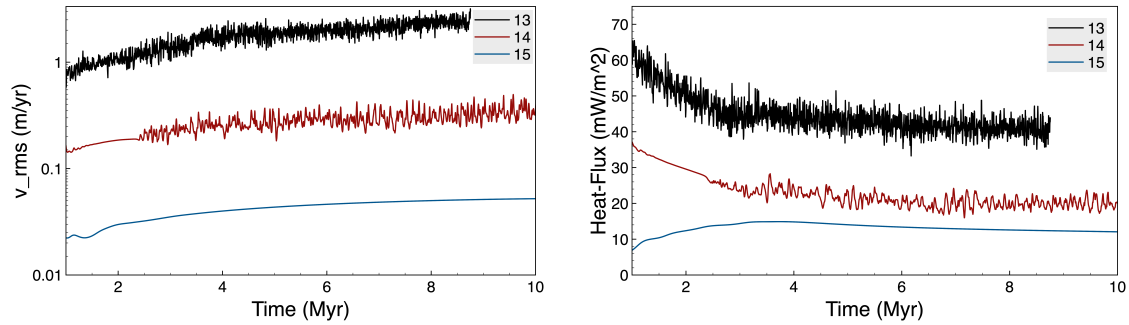

Figure 2.3: Effect of the Initial Viscosity $\eta_0 = 10^{xx}$ Pa s, rms velocity (left) and bottom heat flux (right) time evolution

In the left panel of Figure 2.3, it is again important to note the log values on the y-axis. In the left panel again of Figure 2.3, the values 13, 14, 15 represent 10^{13}, 10^{14}, and 10^{15} Pa s respectively. Due to the viscosity dependence in the Ra as defined by equation 1.26, as the viscosity increases there is a decrease in the v_{rms} leading to a less efficient flow. This is evident in the 10^{15} Pa s simulation where the v_{rms} is significantly lower than the 10^{14} Pa s simulation and even 10^{13} Pa s simulation.

In the right panel of Figure 2.3, it is also noticeable the higher the viscosity value such as the 10^{15} Pa s, less heat is extracted from the ocean compared to

the 10^{13} Pa s and 10^{14} Pa s cases. This is also due to the lower Ra value.

In conclusion, the larger thickness (D), the more vigorous the convective flow. On the other hand, the larger initial ice viscosity value (η_0), the less vigorous the convective flow becomes. Also, less heat is transferred by the ice crust.

2.2 Thermal Convection in a Thickening Crust

The previous section dealt with analyzing changing parameters in comparison with a reference configuration. Now, the focus will be on a variable thickness ice crust (D) with a constant initial viscosity (η_0) parameter, and heat flux (q_s) supplied by a silicate core. Later in the section, will focus on the effect of presence of ammonia on the ocean/ice crust interface.

2.2.1 Effect of Internal Heat Flux

In this section, an assumption is made there is no ammonia in Titan's ocean and will primarily investigate the effects of variable q_s on the thickness of the ice crust. The question of ammonia and HP ice will be addressed in sections 2.2.2, and 2.2.3. In Figure 2.4, the simulation used a constant initial viscosity $\eta_0 = 10^{14}$ Pa s.

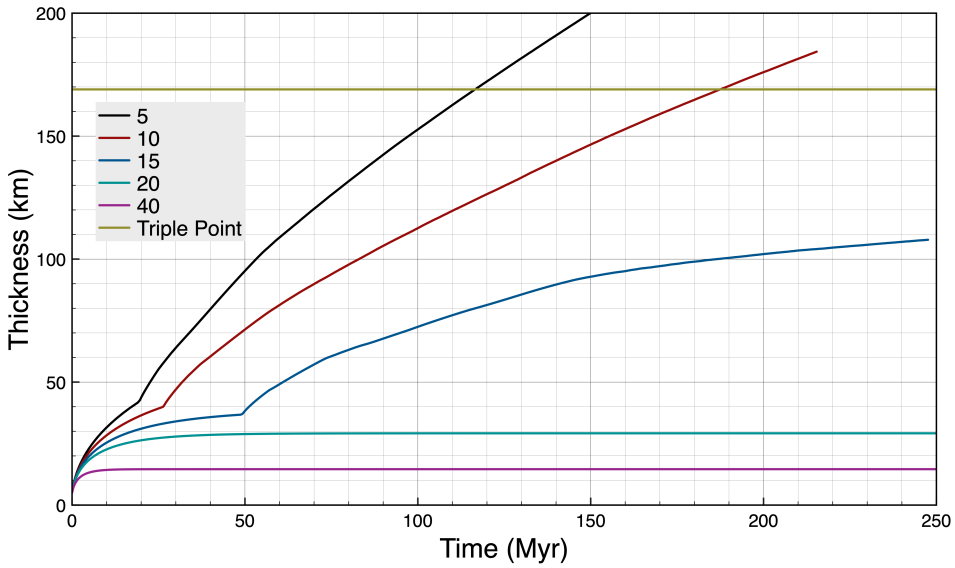

Figure 2.4: Effect of q_s (in mW/m^2) on Ice Crust thickness

In Figure 2.4, it is important to explain the significance of the q_s values. The flat yellow line at the top of Figure 2.4, represents the triple point for H_2O. Thus, when the ice crust reaches this value, the ocean will completely freeze. Near the beginning of Figure 2.4 it is noticeable for all of the heat flux (q_s) values, there is an increase in the thickness. This is a result of $\Delta q > 0$ as defined in 1.3.6, resulting in crystallization. However, note how the heat flux (q_s) values of 20, 40 mW/m^2, have an increase then have a constant thickness, this will be explained in a later paragraph. Also, in all the thin crusts the heat is transferred by conduction explaining why the lines are on top of each other initially.

Looking at the lower heat flux (q_s) values, 5 - 15 mW/m^2, in Figure 2.4, these are the current expected values of the heat flux produced by Titan's silicate core (cf. Figure 1.14). Also, note the smooth curve then the sharp increase in the thickness for the 5 - 15 mW/m^2 values, this represents the shift from conduction to convection. For each of the heat flux values, the crust beginsf to convect around the same thickness, roughly 35 - 45 km thick ice crust. It is evident for a q_s values of 5 and 10 mW/m^2, the ocean will completely freeze around 115 Myrs, and 185 Myrs respectively. However, for 15 mW/m^2, the ocean will remain liquid for longer periods as see in Figure 2.4, where after 250 Myrs the crust has a thickness roughly of 110 km.

Now concerning the higher heat flux (q_s) values, 20 and 40 mW/m^2, in Figure 2.4, these are the expected values in the early days of Titan. There is no sharp increase like experienced by the heat flux values of 5 - 15 mW/m^2, as the 20 - 40 mW/m^2 do not experience any convection. This is due to the heat flux (q_s) supplied by the silicate core is equal to the heat flux extracted by the ice (q_i). Since these are equal causing Δq as defined by Section 1.3.6 to be equal to zero. Thus, there is neither crystallization or melting resulting in a crust thickness of approximately 30 km and 15 km for 20 mW/m^2 and 40 mW/m^2 respectively.

Ideally, the long term evolution of the ocean should be investigated by prescribing a time dependent q_s and running the whole 4.6 Gyr evolution. However, such simulations would take too long to compute, especially since convection starts at certain crust thickness (depending mainly on the value of viscosity η_0) which leads to significant decrease in the CFL calculated time step. Figure 2.5 shows the ice crust thickness as a function of time for this kind of simulation. There are three values of initial viscosity: $\eta_0 = 10^{13}$, 10^{14}, and 10^{15} Pa s.

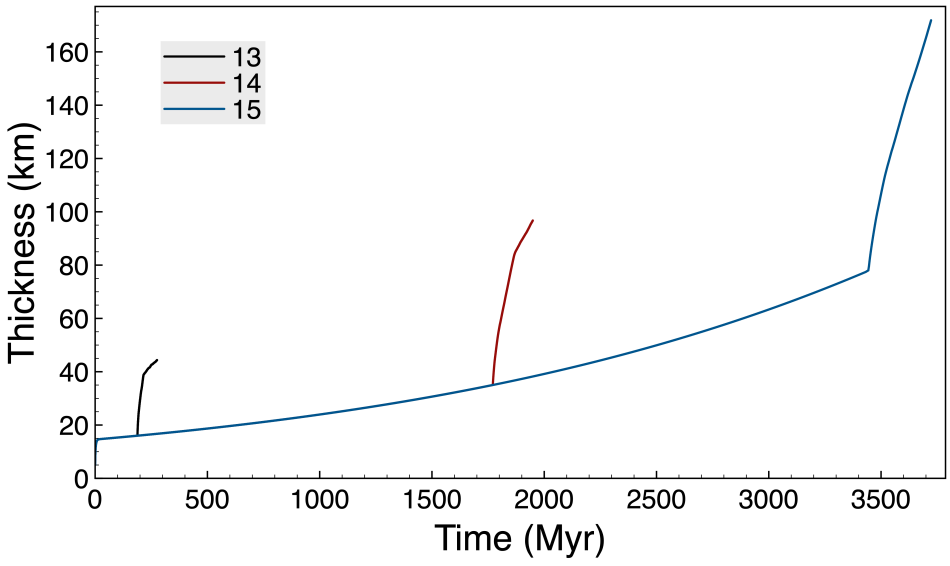

Figure 2.5: Effect of time dependent heat flux q_s on the ice crust thickness with an initial viscosity $\eta_0 = 10^{xx}$ Pa s

q_s in the previous Figure 2.5 is defined as the following equation:

$$q_s = q_{s_0} e^{-t/2000}. \tag{2.1}$$

Where in Equation 2.1, t is in Myrs and $q_{s_0} = 40$ mW/m^2. The equation 2.1 approximates the blue line in Figure 1.14. In Figure 2.5, for the smallest viscosity (10^{13} Pa s), convection starts around 200 Myrs, where the crust starts to thicken significantly. Increasing the viscosity by a magnitude of 10, (10^{14} Pa s), decreasing the Rayleigh number (Ra) as defined by equation 1.26, convection starts later when the crust is thick enough ($\sim$ 1700 Myrs) and the crust quickly thickens. Finally for the largest tested viscosity (10^{15} Pa s), it takes a significant amount of time ($\sim$ 3500 Myrs) before the crust is thick enough to convect. It would appear in this largest tested case the ice crust begins to convect around 70 km. Even with this largest viscosity value the crust thickness quickly reaches the value of 170 km, corresponding to the ocean being frozen (cf. Figure 2.4). In final, it is evident for smaller viscosities the ocean will freeze in earlier time while in larger viscosities it will freeze later.

Since it is not possible to compute this long term evolution, crystallization is assumed to be very slow during the first $\sim$3 Gyr when the heat flux is large ($>$ 15 mW/m^2). Thus the following sections 2.2.2, and 2.2.3, will focus only on the time evolution when heat flux is small ($<$ 15 mW/m^2).

2.2.2 Effect of Viscosity on Ocean Thickness

As seen in Figure 2.3, different initial viscosities will result in higher flow if the viscosity is lower, or lower flow if the viscosity is higher. Figure 2.6, will analyze three viscosity values (10^{13}, 10^{14}, 10^{15} Pa s) with a constant heat flux of $q_s = 5$ mW/m^2, and an initial ammonia concentration of 0%.

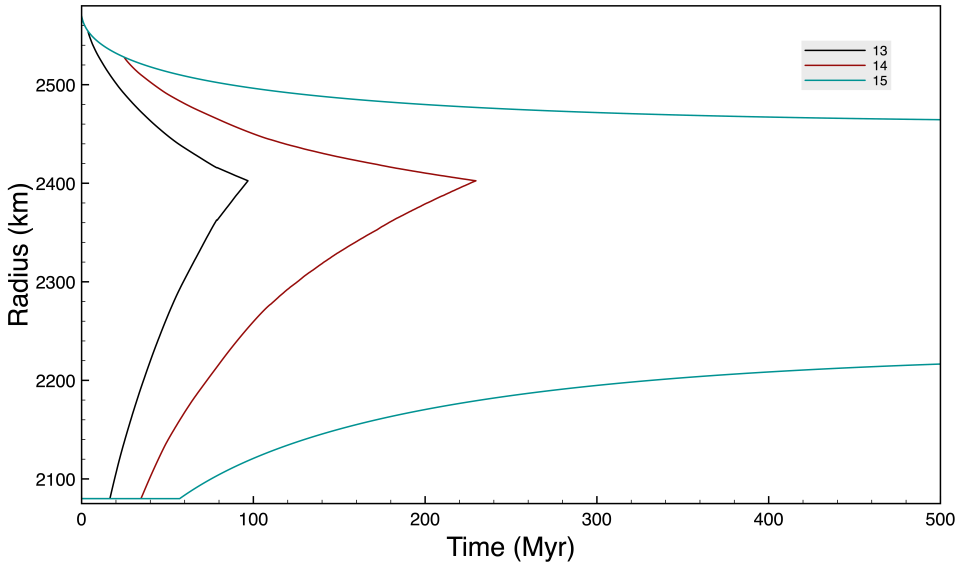

Figure 2.6: Viscosity ($\eta_0 = 10^{xx}$ Pa s), heat flux ($q_s = 5$ mW/m^2) on ocean thickness

Figure 2.6, will be a standard time evolution figure used for the rest of the thesis. To give an understanding of this figure, to the left of the black line, red line, this represents the liquid ocean. Also between the teal lines this represents the ocean. Above the black line, red line, and teal line, this represents the thickness of the Ice I crust. Finally the bottom lines represents the radius of the HP Ice /

ocean interface as defined by the equation 1.46. In the Figure 2.6, the bottom of the Ice I crust has a melting temperature pressure dependence in accordance with equation 1.49. Thus causing the Ice I crust to thicken as the pressure increases, and in turn lowering the melting temperature. At the beginning of each of the simulations, the initial ice crust dimension (D) is set to 5 km.

From Figure 2.6, it is evident the initial viscosity η_0 is important in determining if the ocean will crystalize. As seen with lower viscosity values (10^{13}, 10^{14} Pa s), due to the higher efficiency of heat transfer as a result of the higher Ra, defined by equation 1.26, more heat is extracted from the ocean/ice crust boundary. Thus for a viscosity value equal to 10^{13} and 10^{14} Pa s, the ocean vanishes approximately around 100 Myr, and approximately 230 Myr respectively. However, for viscosity values equal to 10^{15} Pa s, the ocean will be stable on longer term. Thus, justifying the lack of further investigation of the initial viscosity $\eta_0 = 10^{15}$ Pa s in conjunction with initial ammonia concentrations. For the initial viscosity of $\eta_0 = 10^{15}$ Pa s, results in an final ocean thickness of 231 km.

In Figure 2.6, it is clear this is in clear contradiction to Figure 2.5. The reason for this is due to the constant ocean temperature (264 K) in Figure 2.5, compared to a pressure dependent ocean according to Equation 1.49, where the concentration (X) is zero. At the end of Figure 2.6 the ocean temperature is 260 K, low enough to prevent crystallization in the 10^{15} Pa s.

2.2.3 Effect of Composition

This section looks at the effects of two different viscosity values (10^{13}, 10^{14} Pa s), and two heat fluxes (5 mW/m^2, and 10 mW/m^2) with a variable initial concentration of ammonia on the ocean thickness. Note the same time evolution figures will be used as seen the previous section 2.2.2, denoting the top line Ice I crust, the bottom line HP Ice, and left of both lines ocean.

The first figure, Figure 2.7, investigates the effect of different initial concentrations of ammonia on Ice I with a viscosity equal to 10^{13} Pa s and a heat flux equal to 5 mW/m^2.

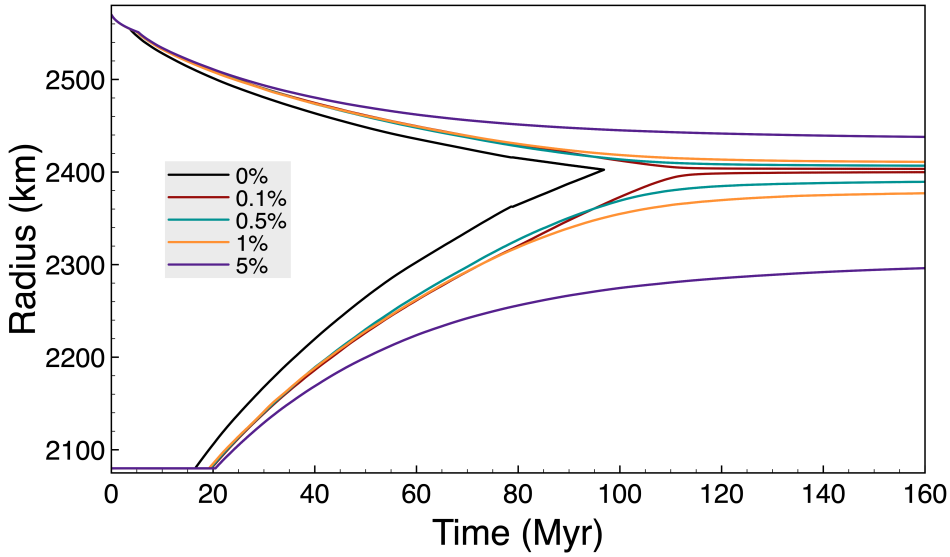

Figure 2.7: Initial parameters ($\eta_0 = 10^{13}$ Pa s, $q_s = 5$ mW/m^2) with variable initial concentration effect on ocean thickness

It is evident in Figure 2.7, with 0% initial ammonia in the ocean, the ocean will quickly freeze, around 100 Myrs. However, with the slightest increase of initial ammonia in the ocean this will prevent the ocean from completely crystalize, thus remaining liquid for long periods of time. Note in the above Figure 2.7, the sharp increase in the Ice I thickness around 10 Myrs. This corresponds to when the crust reaches the critical Ra where it switches from conduction to convection.

As mentioned earlier in section 1.3.7, the ammonia will remain in the ocean, so while the initial concentration will be 1%, the ammonia concentration in the ocean will increase, thus leading to a further decrease in the ice melting temperature as seen in equation 1.49 and visualized in Figure 1.13.

Regarding the 5% initial ammonia concentration, due to the higher initial concentration, the melting temperature at the ocean/crust interface is lower. Thus, slowing the crystalizing rate as seen in Figure 2.7, where the 5% concentration has a longer period without HP Ice compared to the 0%, 0.1%, 0.5%, and 1% cases. Also due to the lower crystallization rate and lower melting temperatures, gives a thicker ocean as seen in Figure 2.7.

Giving some final values for the ocean thickness and ammonia concentrations for the end of the simulation from Figure 2.7, for the initial concentration 0%, the ocean thickness is 0 km and final ammonia concentration of 0%. These values are the same for the next simulations except for Figure 2.10, which will be explained. For the initial ammonia concentration of 0.1%, the final concentration is 14% with an ocean thickness of 3 km. Also, for the simulation of initial concentration of 0.5%, the final concentration is 15% and an ocean thickness of 15 km. Regarding the 1%, the final ammonia concentration is 16%, with a final thickness of 30 km. Finally for the initial concentration of 5%, the final concentration is 18%, and the thickness of 129 km.

In the next figure, Figure 2.8, will investigate the effect of increased heat flux to 10 mW/m^2.

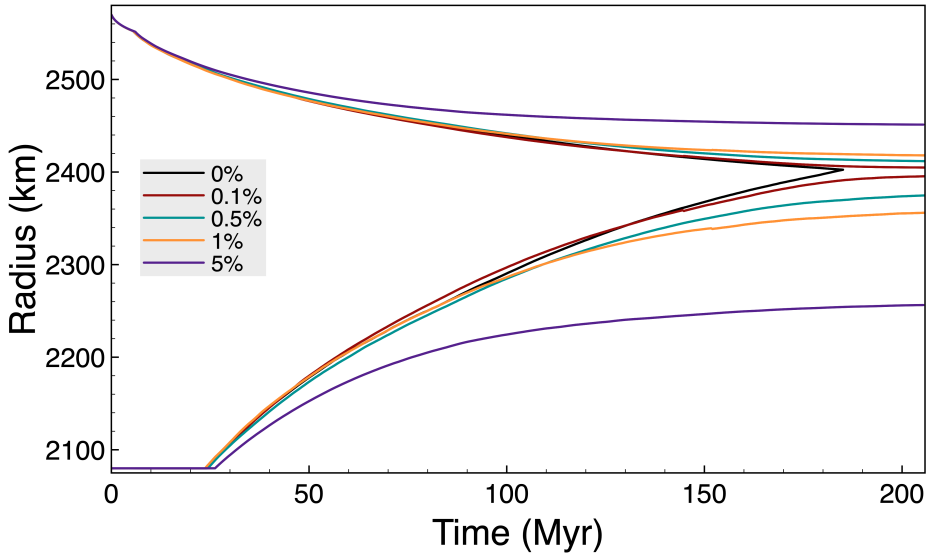

Figure 2.8: Initial parameters ($\eta_0 = 10^{13}$ Pa s, $q_s = 10$ mW/m^2) with variable initial concentration effect on ocean thickness

In Figure 2.8, with the heat flux increased to 10 mW/m^2, the 0% initial ammonia concentration completely crystalizes as seen in 2.4. However when comparing Figure 2.7, and Figure 2.8, it is evident the greater heat flux results in a longer time for the ocean to completely crystalize. Also, 0.1%, 0.5%, 1%, and 5% will have a larger ocean but lower ammonia concentrations. These are evident in the final values for ocean thickness and ammonia concentrations seen in the following paragraph.

For Figure 2.8, the 0.1% initial concentration gives an ocean thickness of 7 km, and final ammonia concentration of 7%. Also for the 0.5% initial concentration gives an ocean thickness of 32 km, and a final concentration of 7%. For the 1% initial concentration has 57 km thick ocean and 8% ammonia concentration. Even for the 5% initial concentration has an ocean thickness of 195 km and a final ammonia concentration of 12%. Thus confirming the conclusion larger oceans result in lower ammonia concentrations.

The next figures, Figure 2.9 and Figure 2.10, will analyze the effects of a higher initial viscosity $\eta_0 = 10^{14}$ Pa s. To start, Figure 2.9 will look at the time evolution of the ocean with a supplied heat q_s of 5 mW/m^2:

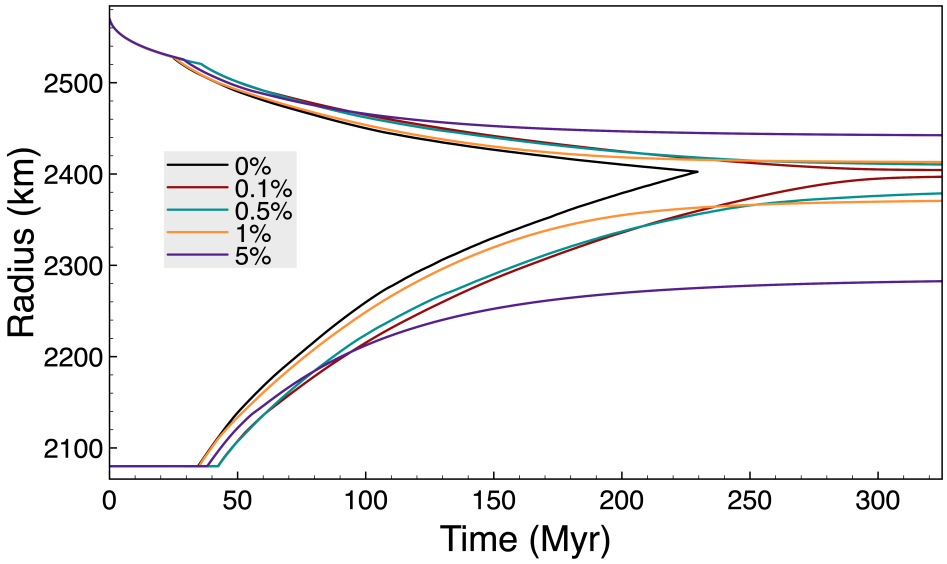

Figure 2.9: Initial parameters ($\eta_0 = 10^{14}$ Pa s, $q_s = 5$ mW/m^2) with variable initial concentration effect on ocean thickness

In Figure 2.9, it is evident when comparing it to Figure 2.7, the 0% initial ammonia concentration in both oceans freezes completely. However an interesting note comes when comparing the time between the complete crystallization. The simulation with $\eta_0 = 10^{14}$ Pa s, ocean completely crystalized around 230 Myrs and for the $\eta_0 = 10^{13}$ Pa s simulation, the ocean crystalizing in about 100 Myrs. This proving the effects of a higher viscosity resulting in longer times for the ocean to completely crystalize as seen in Figure 2.6.

With the higher initial viscosity value, it is expected for all the initial ammonia concentrations for the $\eta_0 = 10^{14}$ Pa s will result in larger oceans compared to the $\eta_0 = 10^{13}$ Pa s as seen in Figure 2.6. This expectation is evident when comparing the two figures, 2.7 vs 2.9. Where the final ocean thickness seen in Figure 2.7 for 0.1%, 0.5%, 1% and 5% is 3 km, 15 km, 30 km, and 129 km respectively, compared to Figure 2.9 for 0.1%, 0.5% 1% and 5% is 5 km, 25 km, 57 km, and 195 km respectively.

When comparing the final ammonia concentration values, it is expected the larger ocean in the $\eta_0 = 10^{14}$ Pa s simulation to the $\eta_0 = 10^{13}$ Pa s, the ammonia concentration values will be lower. This is evident when looking at the values in the $\eta_0 = 10^{13}$ Pa s where for the initial concentrations of 0.1%, 0.5%, 1% and 5%, the final concentrations are 14%, 15%, 16% and 18% respectively. Compared to the $\eta_0 = 10^{14}$ Pa s case when the 0.1%, 0.5%, 1%, and 5% initial concentrations have final concentrations of 9%, 9%, 12% and 15% respectively. Thus confirming again the idea of large ocean resulting in smaller final ammonia concentrations comparably.

In the final figure, Figure 2.10, will investigate the effect of an increased heat supplied from the silicate core to 10 mW/m^2.

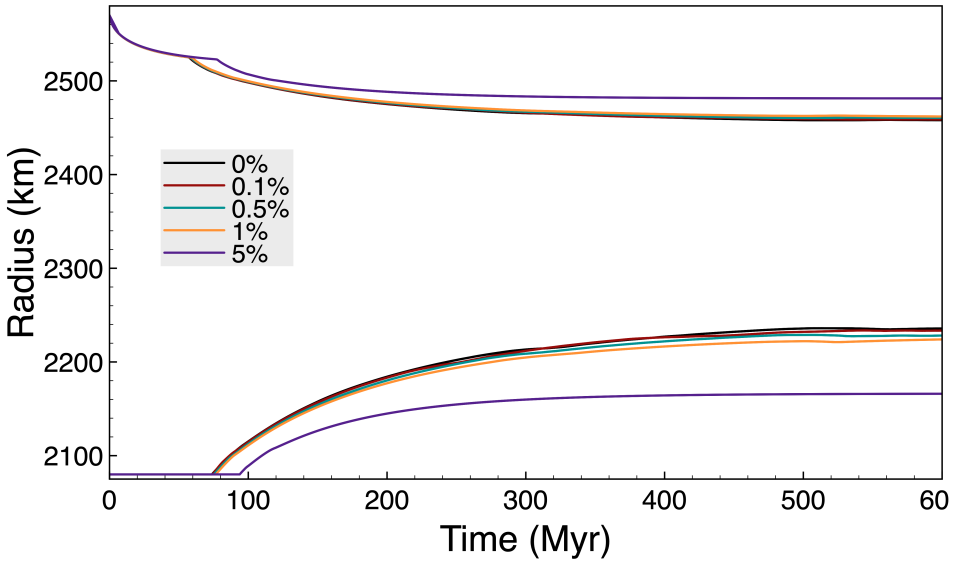

Figure 2.10: Initial parameters ($\eta_0 = 10^{14}$ Pa s, $q_s = 10$ mW/m^2) with variable initial concentration effect on ocean thickness

In Figure 2.10, it is evident all values of ammonia concentration result in a thick ocean, even with the initial ammonia concentration of 0% simulation. This shows the strong influence of heat flux coupled with a higher initial viscosity value, giving a long term stable ocean.

Comparing this Figure 2.10 to Figure 2.9, it is expected for the final ocean thickness to be larger. This is evident when looking at the thickness seen in Figure 2.10 for the initial concentrations of 0.1%, 0.5%, 1% and 5% results in a final ocean thickness for 223 km, 232 km, 237 km and 315 km respectively. Comparing these values to Figure 2.8, for the initial concentrations of 0.1%, 0.5%, 1%, and 5%, 7 km, 32 km and 57 km, and 195 km for $\eta_0 = 10^{13}$ Pa s with a supplied heat flux of 10 mW/m^2, it is evident the greater viscosity results in a thicker ocean.

The final ammonia concentrations, for the simulations represented above in Figure 2.10 are 0.2%, 1%, 2% and 8% for initial concentrations of 0.1%, 0.5%, 1%, and 5% respectively. These values are reasonable due to the thicker ocean as seen in the values represented in the previous paragraph.

Below in Table 2.1 are the results regarding final ocean thickness and ammonia concentrations for the previous figures.

	$\eta_0 = 10^{13}$ Pa s			
q_s (mW/m^2)	5		10	
$X_0 = 0$ %	0 km	0%	0 km	0%
$X_0 = 0.1$ %	3 km	14%	7 km	7%
$X_0 = 0.5$ %	15 km	15%	32 km	7%
$X_0 = 1$ %	30 km	16%	57 km	8%
$X_0 = 5$ %	129 km	18%	195 km	12%
	$\eta_0 = 10^{14}$ Pa s			
q_s (mW/m^2)	5		10	
$X_0 = 0$ %	0 km	0%	216 km	0%
$X_0 = 0.1$ %	5 km	9%	223 km	0.2%
$X_0 = 0.5$ %	25 km	9%	232 km	1%
$X_0 = 1$ %	40 km	12%	237 km	2%
$X_0 = 5$ %	156 km	15%	315 km	8%

Table 2.1: Comparison of final ocean thickness and ammonia concentrations

As seen in Table 2.1, for both supplied heat values with the initial concentrations of 0% ammonia, the ocean completely freezes except for $\eta_0 = 10^{14}$ Pa s and $q_s = 10$ mW/m^2. A small increase in the ammonia as seen in the 0.1% cases prevents the ocean from freezing. As also seen in Figure 2.4, an increase in the supplied heat (q_s) leads to a larger, stable ocean for longer periods of time. Also noticeable in the Table 2.1, is the significant increase in the ammonia in the ocean, due to the ammonia staying in the ocean as defined in Section 1.3.7. Thus, the size of the ocean is proportional to the precent amount of ammonia in the ocean.

In Table 2.1, as shown above in Figure 2.6, the q_s equal to 5 mW/m^2 for both viscosities ($\eta_0 = 10^{13}$ Pa s, $\eta_0 = 10^{14}$ Pa s) the ocean completely freezes if no ammonia is present. However, an interesting result coming from the model shows with a supplied heat equal to 10 mW/m^2 and initial viscosity equal to $\eta_0 = 10^{14}$ Pa s, the ocean is stable in the long term. This corresponds to Figure 2.6, with a higher initial viscosity brings a thick stable ocean in the long term. Thus showing the importance of viscosity and supplied heat if the initial ammonia percentage in the ocean is equal to zero to prevent the ocean to freezing.

3. Discussion

The results presented in Table 2.1 encompass a large range of ocean thicknesses and ammonia concentrations. We will try to narrow down this range by using the constraints coming from the published literature.

Concerning the ocean thickness, we can obtain a range of possible values by using Equation 1.46 together with the estimates of ice I thickness and the hydrosphere thickness. The total hydrosphere thickness can be obtained as a difference between the radius of Titan (2575 km) and the radius of the silicate core (2080 km), thus giving about 495 km. The minimum estimated ice crust thickness is about 65 km (*Béghin et al.*, 2012). Thus the maximum thickness must be below 170 km as this corresponds to the triple point of ice I - ice III - liquid (a completely crystallized ocean). For D = 65 km, there would be no HP ice and thus the ocean thickness would be 495 km - 65 km = 430 km. For D = 150 km, there would be about 255 km of HP ice and the ocean thickness would be 495 km - 150 km - 255 km = 90 km. We therefore can assume the ocean will be between 90 and 430 km thick.

The ammonia concentration in Titan's ocean is not known but cannot be too high as the ammonia content significantly lowers the liquid density (*Croft et al.*, 1988). Thus, the expected ocean density values of Titan are between 1100 and 1300 kg/m^3, derived from the Cassini data (*Mitri et al.*, 2014). Moreover, a recent study by *Leitner and Lunine* (2019) found the current ammonia concentrations in the ocean cannot be larger than 5%.

Comparing these estimates with the values listed in Table 2.1, we can see the simulations with relatively high heat flux of 10 mW/m^2 (corresponding to CI composition of the core, cf. Figure 1.14) and the larger estimate of ice viscosity of 10^{14} Pa s would give results compatible with our current understanding of Titan's interior. Similarly, an even larger viscosity of 10^{15} Pa s would lead to ocean thickness of 231 km, which is compatible with the data for a smaller heat flux of 5 mW/m^2 (cf. Figure 2.6). Alternatively, the layer of low conductivity material on top of Titan's crust (*Tobie et al.*, 2006) could help to keep the ocean liquid on long timescales even for smaller values of heat flux and viscosity. However, this development is out of the scope of this present thesis.

The model developed in this thesis uses several simplifications such as Newtonian viscosity and Cartesian geometry. While ice viscosity is in general highly nonlinear (cf. Section 1.2.4), the main convective part likely deforms by linear diffusion creep while the nonlinear creeps are dominant in the boundary layers and the stagnant lid. Therefore, using equation 1.30 provides a reasonable first order estimate. The use of Cartesian geometry results in slight underestimation of the extracted basal heat flux with respect to the spherical solution. However, this error is on the order of a few percent and can thus be neglected in the view of larger uncertainty in other parameters (η_0, q_s).

In this thesis, we have shown a subsolidus convection plays a significant role in the thermal evolution of Titan by efficiently transferring heat from the interior to the surface. Apart from heat, volatiles such as argon that was detected in Titan's atmosphere (*Niemann et al.*, 2010), can be transferred by flowing ice. With the convective velocities on the order of 0.01-5 m/yr (cf. Figure 2.3), the travel times

through a 100 km thick convecting ice layer would be between 20 kyr and 10 Myr, short when compared to the overall time of Titan's evolution. While the presence of the stagnant lid on top of the convecting ice layer seems to prevent their release into the atmosphere, processes such as impacts or cryovolcanism could temporarily break the stagnant lid and enable the gas to release into the atmosphere. However, a quantitative model of such processes is out of the scope of the present thesis.

Conclusion

In this thesis, a model of the heat transfer through a crystallizing ice crust of Titan was developed. In Section 1, the balance equations were modified into a Stokes formulation and the energy balance by using a Boussinesq Approximation, and scaling analysis. Thus the two parameters, viscosity (η) and thermal conductivity (k), found in the modified balance equations could add significant variability, thus leading the importance of understanding these two. The model was confirmed by the Blankenbach benchmark test in which we verified the implementation of thermal convection with a constant and temperature dependent viscosity. Finally, we implemented a thickening ice crust by the Stephan problem.

In Section 2, the model showed the importance of the thickness (D) and viscosity (η) on the Rayleigh number (Ra) and thus on the flow efficiency and convection regime of the ice crust. Then by implementing the interior heat flux, it was shown for small values (5 - 10 mW/m^2) and a pure H_2O ocean, the ocean will freeze within a few hundred Myrs. However, for larger values ($>$ 20 mW/m^2), the ocean is potentially stable on longer timescales. However, the large heat flux will decrease to $\lesssim$ 15 mW/m^2 in $\lesssim$ 3 Gyrs, thus causing the ocean to freeze. When looking at a pure ocean with three different viscosity values (10^{13}, 10^{14}, 10^{15} Pa s) with a pressure dependent melting temperature, shows the ocean will freeze in 100 Myrs, and 250 Myrs for 10^{13}, 10^{14} Pa s respectively. However for larger viscosity values, the ocean is stable on longterm preventing the ocean from crystalizing. Finally, implementing a pressure and initial ammonia concentration dependent melting temperature, the importance of viscosity (η) and heat-flux (q_s) is shown. Thus considering the current knowledge of Titan, an ocean thickness varying between 90 km and 430 km thick, would give a large value for viscosity ($\geq 10^{14}$ Pa s) are necessary to keep the ocean liquid, unless an other mechanism is present to prevent its freezing.

Bibliography

Alnæs, M., J. Blechta, J. Hake, A. Johansson, B. Kehlet, A. Logg, C. Richardson, J. Ring, M. E. Rognes, and G. N. Wells (2015), The FEniCS Project Version 1.5, *Archive of Numerical Software*, *3*, doi:10.11588/ans.2015.100.20553.

Arnold, D. N., F. Brezzi, and M. Fortin (1984), A stable finite element for the Stokes equations, *Calcolo*, *21*, 337–344, doi:10.1007/BF02576171.

Baland, R.-M., G. Tobie, A. Lefevre, and T. V. Hoolst (2014), Titan's internal structure inferred from its gravity field, shape, and rotation state, *Icarus*, *237*, 29 – 41, doi:10.1016/j.icarus.2014.04.007.

Béghin, C., O. Randriamboarison, M. Hamelin, E. Karkoschka, C. Sotin, R. C. Whitten, J.-J. Berthelier, R. Grard, and F. Simoes (2012), Analytic theory of Titan's Schumann resonance: Constraints on ionospheric conductivity and buried water ocean, *Icarus*, *218*(2), 1028 – 1042, doi:10.1016/j.icarus.2012.02.005.

Blankenbach, B., F. Busse, U. Christensen, L. Cserepes, D. Gunkel, U. Hansen, H. Harder, G. Jarvis, M. Koch, G. Marquart, D. Moore, P. Olson, H. Schmeling, and T. Schnaubelt (1989), A benchmark comparison for mantle convection codes, *Geophysical Journal International*, *98*(1), 23–38, doi:10.1111/j.1365-246X.1989.tb05511.x.

Choblet, G., G. Tobie, C. Sotin, M. Běhounková, O. Čadek, F. Postberg, and O. Souček (2017), Powering prolonged hydrothermal activity inside Enceladus, *Nature Astronomy*, *12*, 841–847, doi:10.1038/s41550-017-0289-8.

Croft, S., J. Lunine, and J. Kargel (1988), Equation of state of ammonia-water liquid: Derivation and planetological applications, *Icarus*, *73*(2), 279 – 293, doi:10.1016/0019-1035(88)90098-X.

Durante, D., D. Hemingway, P. Racioppa, L. Iess, and D. Stevenson (2019), Titan's gravity field and interior structure after Cassini, *Icarus*, *326*, 123–132, doi:10.1016/j.icarus.2019.03.003.

Goldsby, D. L., and D. L. Kohlstedt (2001), Superplastic deformation of ice: Experimental observations, *Journal of Geophysical Research: Solid Earth*, *106*(B6), 11,017–11,030, doi:10.1029/2000JB900336.

Grasset, O., and C. Sotin (1996), The Cooling Rate of a Liquid Shell in Titan's Interior, *Icarus*, *123*(1), 101–112, doi:10.1006/icar.1996.0144.

Hobbs, P. V. (1974), *Ice Physics*, 837 pp., Oxford, Clarendon Press.

Hörst, S. M. (2017), Titan's atmosphere and climate, *Journal of Geophysical Research: Planets*, *122*(3), 432–482, doi:10.1002/2016JE005240.

Hudleston, P. J. (2015), Structures and fabrics in glacial ice: A review, *Journal of Structural Geology*, *81*, 1–27, doi:10.1016/j.jsg.2015.09.003.

Iess, L., N. J. Rappaport, R. A. Jacobson, P. Racioppa, D. J. Stevenson, P. Tortora, J. W. Armstrong, and S. W. Asmar (2010), Gravity field, shape, and moment of inertia of Titan, *Science*, *327*(5971), 1367–1369, doi:10.1126/science.1182583.

Iess, L., R. A. Jacobson, M. Ducci, D. J. Stevenson, J. I. Lunine, J. W. Armstrong, S. W. Asmar, P. Racioppa, N. J. Rappaport, and P. Tortora (2012), The tides of Titan, *Science*, *337*(6093), 457–459, doi:10.1126/science.1219631.

Kalousová, K., and C. Sotin (), Dynamics of Titan's high-pressure ice layer, *Earth Planet. Sci. Lett.*, *under review*.

Kvorka, J., O. Čadek, G. Tobie, and G. Choblet (2018), Does Titan's long-wavelength topography contain information about subsurface ocean dynamics?, *Icarus*, *310*, 149–164, doi:10.1016/j.icarus.2017.12.010.

Leitner, M. A., and J. I. Lunine (2019), Modeling early Titan's ocean composition, *Icarus*, *333*, 61–70, doi:10.1016/j.icarus.2019.05.008.

Leliwa-Kopystyński, J., M. Maruyama, and T. Nakajima (2002), The water–ammonia phase diagram up to 300 MPa: Application to icy satellites, *Icarus*, *159*(2), 518–528, doi:10.1006/icar.2002.6932.

Logg, A., K.-A. Mardal, and G. Wells (Eds.) (2012), *Automated Solution of Differential Equations by the Finite Element Method*, *Lecture Notes in Computational Science and Engineering*, vol. 84, Springer-Verlag Berlin Heidelberg, doi:10.1007/978-3-642-23099-8.

Martinec, Z. (2011), Continuum mechanics, *Lecture notes*, http://geo.mff.cuni.cz/studium/Martinec-ContinuumMechanics.pdf.

Matyska, C. (2005), Mathematical introduction to geothermics and geodynamics, *Lecture notes*, http://geo.mff.cuni.cz/studium/Matyska-MathIntroToGeothermicsGeodynamics.pdf.

Mitri, G., R. Meriggiola, A. Hayes, A. Lefevre, G. Tobie, A. Genova, J. I. Lunine, and H. Zebker (2014), Shape, topography, gravity anomalies and tidal deformation of Titan, *Icarus*, *236*, 169 – 177, doi:10.1016/j.icarus.2014.03.018.

Niemann, H. B., S. K. Atreya, J. E. Demick, D. Gautier, J. A. Haberman, D. N. Harpold, W. T. Kasprzak, J. I. Lunine, T. C. Owen, and F. Raulin (2010), Composition of Titan's lower atmosphere and simple surface volatiles as measured by the Cassini-Huygens probe gas chromatograph mass spectrometer experiment, *Journal of Geophysical Research: Planets*, *115*(E12), doi:10.1029/2010JE003659.

Sotin, C., G. Tobie, J. Wahr, and W. McKinnon (2009), *Tides and Tidal Heating on Europa (in Europa, eds Pappalardo, McKinnon, Khurana)*, p. 85, University of Arizona Press.

Stofan, E. R., C. Elachi, J. I. Lunine, R. D. Lorenz, B. Stiles, K. L. Mitchell, S. Ostro, L. Soderblom, C. Wood, H. Zebker, S. Wall, M. Janssen, R. Kirk, R. Lopes,

F. Paganelli, J. Radebaugh, L. Wye, Y. Anderson, M. Allison, R. Boehmer, P. Callahan, P. Encrenaz, E. Flamini, G. Francescetti, Y. Gim, G. Hamilton, S. Hensley, W. T. K. Johnson, K. Kelleher, D. Muhleman, P. Paillou, G. Picardi, F. Posa, L. Roth, R. Seu, S. Shaffer, S. Vetrella, and R. West (2007), The lakes of Titan, *Nature*, *445*, 61–64, doi:10.1038/nature05438.

Taylor, C., and P. Hood (1973), A numerical solution of the navier-stokes equations using the finite element technique, *Computers and Fluids*, *1*(1), 73–100, doi:10.1016/0045-7930(73)90027-3.

Tobie, G., J. I. Lunine, and C. Sotin (2006), Episodic outgassing as the origin of atmospheric methane on Titan, *Nature*, *440*, 61–64, doi:10.1038/nature04497.

Yung, Y. L., M. Allen, and P. J. P. (1984), Photochemistry of the atmosphere of Titan: comparison between model and observations, *Astrophysical Journal Supplement Series*, *55*, 465–506, doi:10.1086/190963.

List of Figures

List of Tables